Economic Geology, v. 100, pp. 935–961

Mineralogical and Isotopic Zonation in the Sur-Sur Tourmaline Breccia, Río Blanco-Los Bronces Cu-Mo Deposit, Chile: Implications for Ore Genesis*

Peter H. Frikken,† David R. Cooke,

Centre for Excellence in Ore Deposits, University of Tasmania, Private Bag 79, Hobart, Tasmania, 7001, Australia

John L. Walshe,

CSIRO, Exploration and Mining, 26 Dick Perry Ave, Kensington, Perth Western Australia 6151, Australia

Doug Archibald,

Department of Geological Sciences and Geological Engineering, Queens University, Kingston, Ontario, Canada K7L3N6

Jorge Skarmeta,

CODELCO-Chile, Gerencia Exploraciones, Santiago, Chile

Luis Serrano, and Ricardo Vargas

CODELCO-Chile, Division Andina, Saladillo, Chile

Abstract

The Sur-Sur tourmaline breccia is located in the southeast part of the Río Blanco-Los Bronces porphyry copper-molybdenum deposit, central Chile. The breccia hosts approximately one-quarter of the total resource of 57 Mt of fine copper at Río Blanco. The breccia is hosted within, and contains altered clasts of, granodiorite from the 12 to 8 Ma San Francisco batholith, which intruded a sequence of Miocene volcanic and volcaniclastic rocks. A series of weakly mineralized to barren felsic porphyries cut the breccia and indicate a minimum age of approximately 6 Ma for mineralization at Sur-Sur.

The Sur-Sur breccia dike is at least 3 km long, 0.2 km wide, and has a vertical extent of at least 1 km. The breccia has been cemented by early biotite and anhydrite at depth and by tourmaline and specularite at higher altitudes. These early-formed cements have been overgrown and in some cases replaced by chalcopyrite, magnetite, pyrite, and quartz. Mineralogical zonation in the breccia includes a transition from biotite cement and related biotite alteration upward to tourmaline cement and quartz-sericite-tourmaline alteration at approximately 3,000-m elevation. Iron-oxide minerals are also zoned, with a transition upward from a magnetite-dominated zone below 3,330 m to a specularite-dominated zone above 3,600 m. Pyrite is the dominant sulfide at altitudes above 4,000 m.

Secondary liquid-rich, vapor-rich, and hypersaline fluid inclusions are preserved in quartz and tourmaline cement. Measured homogenization temperatures are mostly between 300° and 450°C, and salinities range from 0 to 69 wt percent NaCl equiv. Sulfur isotope compositions of sulfide cement range from –4.1 to +2.7 per mil. The lowest $\delta^{34}S_{(sulfide)}$ values are in samples from between 3,700- and 4,000-m elevation, where they correspond to the highest copper grades in the tourmaline breccia. This high-grade zone also contains abundant specularite (locally replaced by magnetite). Modeling of sulfate-sulfide equilibrium indicate that approximately 150°C of cooling over a vertical interval of 100 m would be required to account for the zonation of sulfide isotope compositions at Sur-Sur, making conductive cooling an unlikely ore-forming mechanism.

Measured $^{206}Pb/^{204}Pb$ values of lead in anhydrite cement in the Sur-Sur tourmaline breccia and the Río Blanco magmatic breccia range from 17.558 to 18.479. $^{207}Pb/^{204}Pb$ values range from 15.534 to 15.623, and $^{208}Pb/^{204}Pb$ values range from 37.341 to 38.412. The lead in anhydrite is considerably less radiogenic than that indicated by values obtained previously for lead in sulfide ores and igneous host rocks at Río Blanco-Los Bronces. The source of lead in anhydrite must have been from rocks external to the main magmatic-hydrothermal system, probably the Precordilleran basement.

A magmatic-hydrothermal explosion from a deep-seated crystallizing intrusion triggered breccia formation at Sur-Sur. Hydrostatic pressures catastrophically exceeded lithostatic load plus the tensile strength of the confining granodiorite, leading to widespread brecciation and subsequent invasion by large volumes of magmatic gas and hypersaline brine. The low-density gas phase (carrying H_2O, SO_2, HCl, and B_2O_3) separated physically from the dense copper-bearing brine and flushed through the breccia column first, where it condensed into ground waters of uncertain derivation. Anhydrite, specularite, and tourmaline were deposited from this low-salinity, acidic, oxidized hybrid solution. Subsequent upwelling of magmatic-hydrothermal brine resulted in sulfide deposition. High-grade copper deposition is interpreted to have occurred in response to mixing of the oxidized, acidic water with the copper-bearing magmatic-hydrothermal brine.

† Corresponding author: e-mail, pfrikken@utas.edu.au

*Appendices 1 and 2 are electronically available at <www.segweb.org/EG/papers/Abs100-5_files/07FrikkenAppendix.pdf>

0361-0128/05/3529/935-27 $6.00

Introduction

The Río Blanco-Los Bronces breccia-hosted copper-molybdenum deposit is located 80 km northeast of Santiago in the Chilean Andes (lat 33°09'; Fig. 1). It is the world's third-largest porphyry copper deposit, with a resource of 6.99 billion metric tons (Gt) at 0.75 percent copper, 0.018 percent molybdenum, and 0.035 g/t gold, which equates to 56.73 million metric tons (Mt) of fine copper (Camus, 2002). Mineralized breccias in the central (Río Blanco) and southeastern (Sur-Sur) sectors are being mined currently by CODELCO (Andina Division), whereas the northwestern part of the ore deposit (Los Bronces) is an Anglo American mining operation (Fig. 1). The Andina mining operation exploits two styles of mineralized breccia: the Río Blanco biotite-cemented breccia (known as the "magmatic breccia") located in the center of the ore deposit, and the 3-km-long Sur-Sur tourmaline breccia, which occurs above and to the southeast of the biotite-cemented breccia and incorporates the Don Luis and Sur-Sur mining sectors (Fig. 1).

Río Blanco-Los Bronces has been the subject of several geological and geochemical investigations. Warnaars et al. (1985) provided the first comprehensive descriptions of the mineralized breccias, with additional descriptions provided in Serrano et al. (1996). Vargas et al. (1999) was the first to document mineralogical zonation in the Sur-Sur breccia complex. Skewes et al. (2003) documented the geology of the Donoso breccia at Los Bronces. Fluid inclusion investigations of breccia cements from the Río Blanco, Sur-Sur, and La Americana sectors were reported by Kusakabe et al. (1990) and Vargas et al. (1999). Fluid inclusions from Los Bronces were analyzed by Holmgren et al. (1988) and Skewes and Holmgren (1993). Kusakabe et al. (1984, 1990) reported sulfur isotope compositions for sulfate and sulfide minerals from Río Blanco-Los Bronces. Lead isotope compositions were analyzed by Tosdal and Munizaga (1996). Serrano et al. (1996), Skewes and Stern (1996), and also Hollings et al. (2005) analyzed Sr-Nd compositions of rocks and minerals from Río Blanco-Los Bronces. Deckart et al. (2005) determined the timing of mineralization through a detailed U-Pb and Ar-Ar geochronological study. Characteristics of melt and fluid inclusions in the late porphyries have been documented by Davidson and Kamenetsky (2001) and Davidson et al. (2005). However, the processes of ore deposition remain poorly understood. We report here mineralogical and isotopic zonation within the porphyry-related Sur-Sur tourmaline breccia complex and use these results to interpret the processes that caused deposition of high-grade ore. Our work is based on field and petrographic observations of selected drill core, together with sulfur isotope, fluid inclusion, and radiogenic isotope analyses of samples collected through two sections of the Sur-Sur breccia complex. Mineralogical zonation has been compiled from the digital database of CODELCO (Andina Division), which contains results of more than 20 yr of core logging by Andina geologists. We have supplemented this digital database with our own field and petrographic observations.

Geology

The geology of the Río Blanco-Los Bronces deposit is outlined in Figure 1. The geologic setting of the deposit and key geodynamic elements relevant to ore formation have been discussed in detail in Warnaars et al. (1985), Serrano et al. (1996), Vargas et al. (1999), Kay et al. (1999), Frikken (2004), Hollings et al. (2005), and Deckart et al. (2005). A brief description of the geology is provided below.

The Río Blanco-Los Bronces deposit is hosted by Miocene volcanic and volcaniclastic rocks of the moderately deformed Abanico Formation and weakly deformed Farellones Formation (Warnaars et al., 1985; Serrano et al., 1996; Vargas et al., 1999; Hollings et al., 2005). These have been intruded by the late Miocene San Francisco batholith (Vergara et al., 1988; Serrano et al., 1996; Fig. 1). The Río Blanco-Los Bronces deposit occurs within the roof zone of this batholith and the overlying Farellones Formation. Deckart et al. (2005) dated the three phases of the San Francisco batholith at Río Blanco-Los Bronces: Rio Blanco granodiorite (11.96 ± 0.40 Ma), Cascada granodiorite (8.4 ± 0.23 Ma), and Diorite (8.19 ± 0.16 Ma), all of which preceded the main mineralizing events.

In the late Miocene-Pliocene, the San Francisco batholith and the Farellones Formation were intruded by mineralized biotite and tourmaline-cemented breccias and late mineral felsic porphyries (Deckart et al., 2005). Ore in the Río Blanco sector occurs primarily as cement in the Río Blanco magmatic breccia, a biotite-anhydrite-sulfide–cemented magmatic-hydrothermal breccia complex associated with biotite and lesser K-feldspar alteration. Tourmaline breccias host mineralization at Sur-Sur, La Union, Don Luis, and Los Bronces (Fig. 1). The Sur-Sur and Don Luis open pits exploit sulfides that occur as hydrothermal cement in the north-trending Sur-Sur tourmaline breccia. This >3-km-long and up to 300-m-wide tourmaline-cemented breccia has a dikelike morphology (Fig. 1) and is mineralized to depths of at least 1,300 m below the present surface. In addition to tourmaline and sulfides, the Sur-Sur breccia is cemented by Fe oxides, quartz, and anhydrite, and the clasts and adjacent granodiorite have undergone quartz-sericite-pyrite-tourmaline alteration.

A series of postmineral rock-flour breccias were emplaced on the western side of the Sur-Sur tourmaline breccia. The magmatic breccia and the tourmaline breccia were then intruded by weakly mineralized and altered to barren porphyries, stocks, and diatremes, which are described by Davidson et al. (2005). These include dikes of quartz monzonite porphyry (6.32 ± 0.09 Ma) and feldspar porphyry (5.84 ± 0.03 Ma), the Don Luis porphyry stock (5.23 ± 0.07 Ma) and the dacite chimney (4.92 ± 0.09 Ma: all U-Pb age determinations from Deckart et al., 2005). Magmatism at Río Blanco-Los Bronces ceased with emplacement of the La Copa rhyolite complex, a volcanic vent that contains both intrusive and extrusive facies, including diatreme breccias and ignimbrites. The La Copa complex was emplaced at approximately 4.03 ± 0.19 Ma, based on a K-Ar biotite age determination by Quirt et al. (1971).

Sur-Sur Tourmaline Breccia

The tourmaline breccia at Sur-Sur contains a distinctive sequence of hydrothermal minerals that sequentially filled void space and now cement the breccia (Fig. 2). Mineral deposition in the breccia can be grouped into the oxide and the mineralization stages (Fig. 2). Sulfide cement formed during the mineralization stage and comprises the ore at Sur-Sur. A

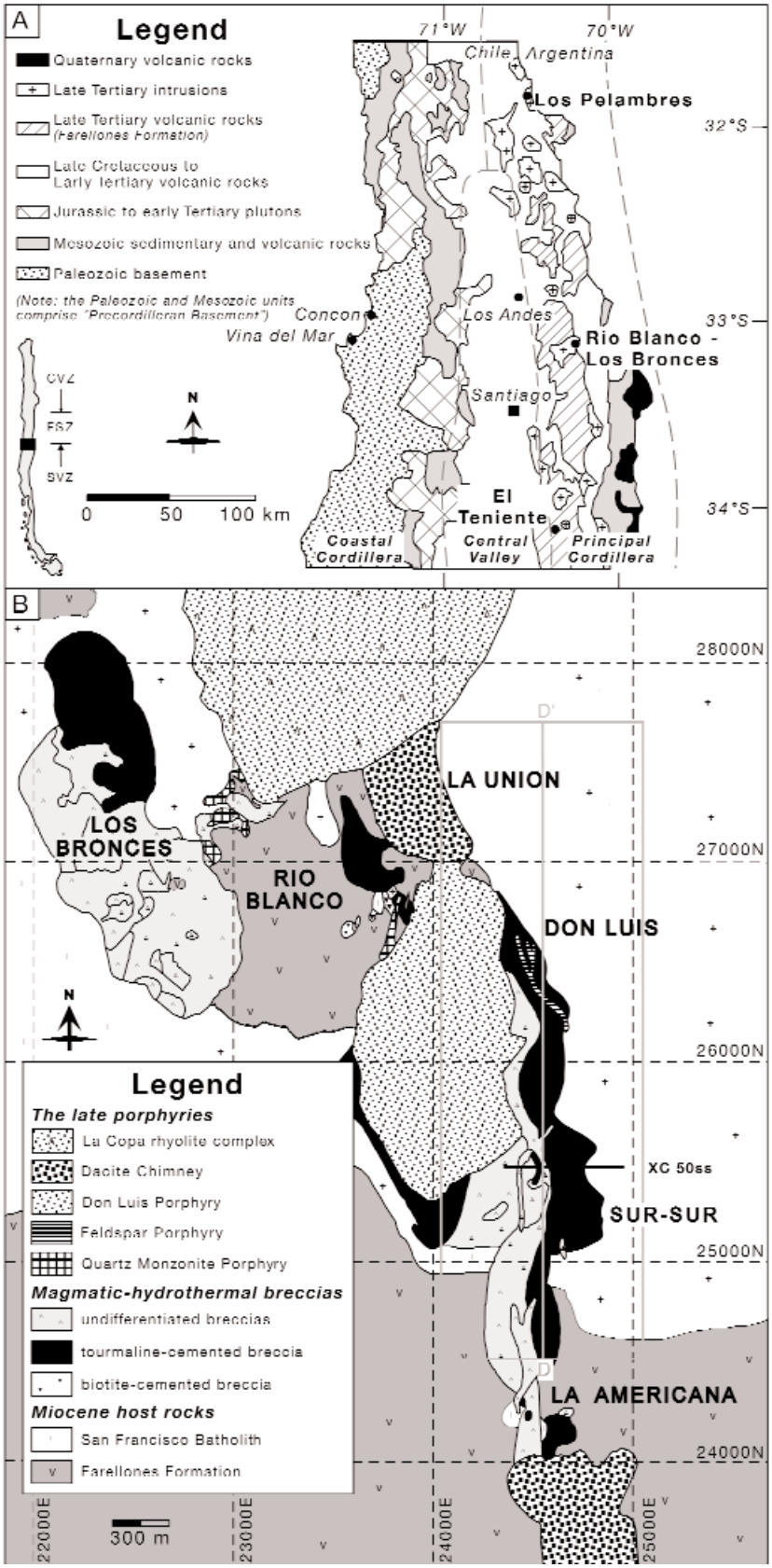

FIG. 1. A. Regional geology of central Chile and location of the Río Blanco-Los Bronces ore deposit (adapted from Serrano et al., 1996). B. Local geology map of Río Blanco-Los Bronces (adapted from Vargas et al., 1999). CVZ = Central volcanic zone, FSZ = Flat Slab zone, SVZ = Southern volcanic zone.

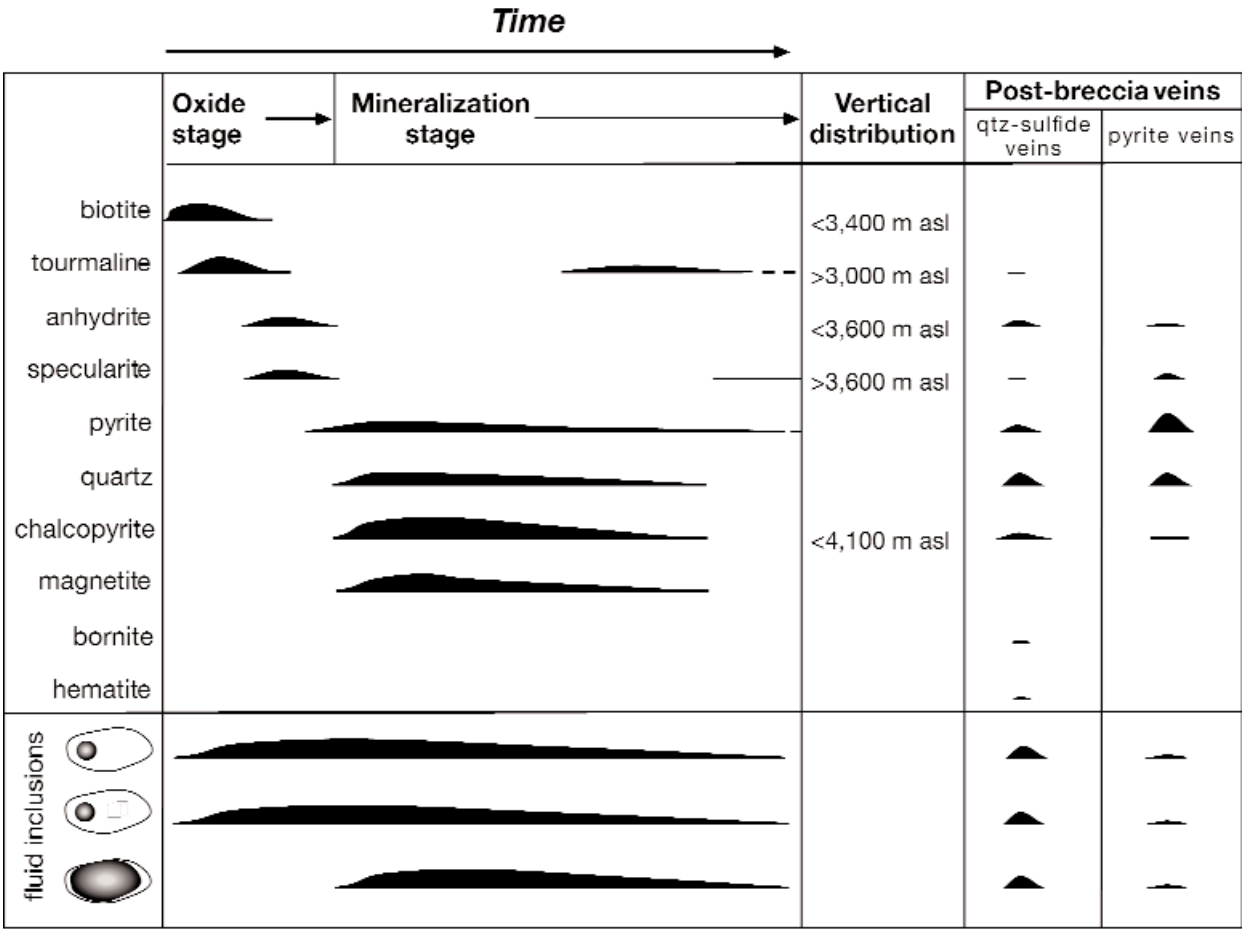

FIG. 2. Infill paragenesis of the Sur-Sur tourmaline breccia, encompassing cement phases deposited during breccia formation and minerals deposited in postbreccia veins. The vertical distribution relates only to the minerals cementing the breccia. Also shown diagrammatically are the three main types of fluid inclusions observed at room temperature in quartz and tourmaline, with respect to the timing of growth of their host minerals. From top to bottom, the fluid inclusion types are (a) two phase, liquid rich undersaturated; (b) three or more phases and hypersaline (contains a halite daughter crystal); (c) two-phase, vapor-rich.

series of weakly mineralized veins have cut the breccia complex and appear to be associated with late porphyry intrusions. The postbreccia mineralization comprises quartz sulfide and pyrite-rich veins.

Oxide stage

The mineralogy of the oxide stage varies with elevation through the Sur-Sur breccia body (Fig. 3). Tourmaline was the first and most abundant cement precipitated in the middle and upper levels of the breccia (Figs. 2–4A, B). Coarse, euhedral tourmaline needles radiate outward from the clast margins (cockade texture; Fig. B, C). The tourmaline needles range in length from 0.1 mm to 1 cm and are generally translucent blue to yellow and green color in plane-polarized light. In some areas, tourmaline also has replaced the margins of altered granodiorite clasts, forming fine-grained tourmaline selvages on the tourmaline cements (Fig. 4B). In the upper parts of the breccia, coarse specularite has overgrown tourmaline and is, in turn, overgrown by sulfide cement (Fig. 4C). The specularite is euhedral and partially fills void space, growing outward from the early-formed tourmaline (Fig. 4C). Early void-filling specularite crystals are up to 3 mm long and 1 mm wide.

Below 3,100-m elevation, the oxide stage is dominated by early-formed biotite and anhydrite (Figs. 2–4D-F, 5A). This part of the Sur-Sur breccia is locally termed the "potassic alteration" domain. There is a transitional zone between 3,000 and 3,100 m where biotite and tourmaline coexist as breccia cement (Fig. 3). Above this zone, tourmaline is the dominant silicate phase. Biotite is the dominant oxide-stage cement below the transitional zone. Only tourmaline and specularite occur above 3,600 m (Fig. 3). Above 3,600-m elevation, anhydrite is absent due to dissolution by modern-day ground waters (Vargas et al., 1999; Figs. 2, 3, 5), and so it is not possible to assess the full vertical extent of cementation by oxide-stage anhydrite.

Mineralization stage

The second stage of void infill was the main-stage mineralization event at Sur-Sur. It involved the deposition of quartz, chalcopyrite, magnetite, pyrite, tourmaline, and minor hematite into open spaces (Figs. 2, 4C, F, 5A-D). Chalcopyrite and

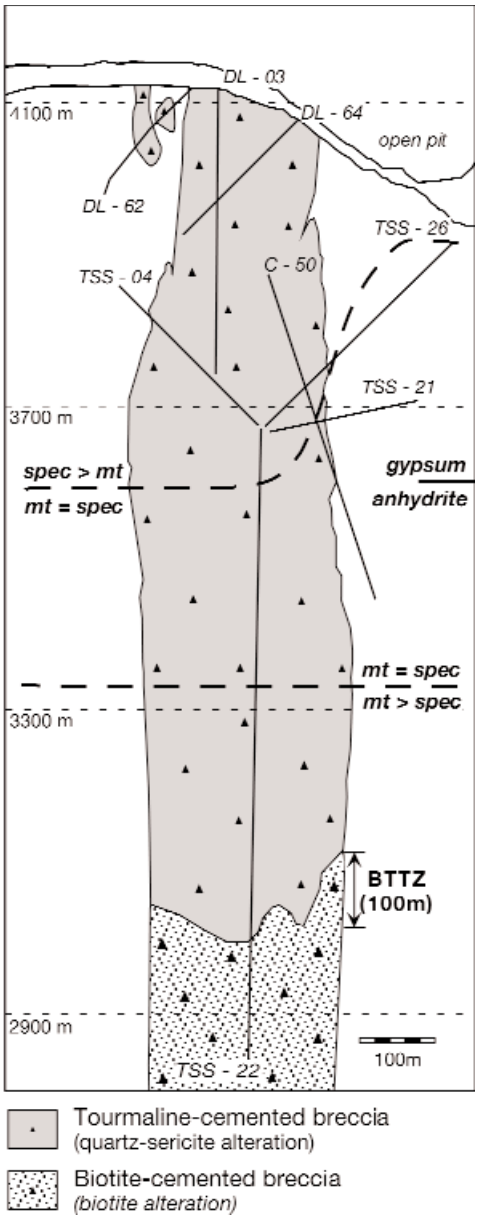

FIG. 3. East-west cross section XC 50ss through the Sur-Sur tourmaline breccia (section location shown in Fig. 1), showing surface and underground diamond drill hole locations used in this study. Filled triangles represent biotite-cemented breccia; unfilled triangles represent tourmaline-cemented breccia. Abbreviations: BTTZ = biotite-tourmaline transition zone, mt = magnetite, spec = specularite, TSS, C, and DL are drill hole labels.

magnetite appear to have been coprecipitated based on textural relationships (e.g., Fig. 5B, C). In the deep levels of the breccia complex, oxide-stage anhydrite crystals have been infilled, and in some cases partially replaced by chalcopyrite associated with the mineralization stage (Figs. 4E, F, 5A). A second generation of tourmaline cement associated with the mineralization stage occurs as fine-grained, equigranular blue and/or black masses and sinuous trails that have cut later formed cements (Fig. 2).

A zonal distribution of the oxide minerals, magnetite, and specularite is evident in section XC 50ss. Magnetite is predominant at elevations below 3,330-m depth (magnetite > specularite; Fig. 3). There is a transitional zone between 3,330 and 3,600 m where the two minerals have similar abundances. A specularite-dominated zone occurs above 3,600 m (specularite > magnetite; Fig. 3) and coincides with an increased abundance of vugs in the breccia. Locally, between 3,600 and 4,000 m above sea level, magnetite forms a pseudomorph after oxide-stage specularite (Fig. 5B-E). This zone corresponds to higher copper grades (<2% Cu). Magnetite does not occur above 4,000-m elevation, where pyrite is the dominant sulfide mineral and specularite coexists with chalcopyrite (Fig. 4C). Incipient supergene alteration has produced thin chalcocite rinds around chalcopyrite grains at high elevations.

Postbreccia veins

After cementation, the tourmaline breccia was cut by a weak stockwork of quartz sulfide veins (Fig. 4B) with quartz-sericite-pyrite alteration halos. These quartz veins contain minor amounts of chalcopyrite, pyrite, bornite, anhydrite, tourmaline, and fine blades of specularite (Fig. 2). At lower elevations in the Sur-Sur breccia, chalcopyrite cement has been partly altered to bornite adjacent to some postbreccia veins. Also, hematite has replaced magnetite cement (Fig. 5F), and fine blades of specularite have been deposited within and surrounding the postbreccia veins.

Late-stage pyrite-rich veins with minor quartz, chalcopyrite, anhydrite, and gypsum, and with quartz sericite alteration halos (analogous to the D veins described from El Salvador by Gustafson and Hunt, 1975) characterize the final phase of vein formation at Rio Blanco-Los Bronces. They cut the tourmaline breccia at Sur-Sur (Fig. 4B). They also cut the chalcopyrite-bearing quartz veins, and all phases of the late porphyries, up to and including the Don Luis porphyry.

Mineral zonation

In addition to the mineral zonation described above, Vargas et al. (1999) recognized a specularite alteration halo, which extends upward and outward gradationally, and a biotite breccia that extends downward from the tourmaline breccia. They also noted that the abundance of pyrite increases upward through the breccia and that pyrite/chalcopyrite ratios increase outward to the margin of the orebody.

We have investigated mineral zonation in the Sur-Sur breccia complex using the digital database of CODELCO Andina Division. The spatial distribution of hydrothermal minerals is plotted on longitudinal section D-D' and cross section XC 50ss (section locations shown in Fig. 1). The drill holes cover an area from the La Americana sector in the south through the Sur-Sur sector to the Don Luis sector in the north (Fig. 1). Drill holes have been projected onto section line D-D' from a distance up to 225 m from either side of the section. A series of longitudinal sections have been prepared to show the spatial distribution of biotite (potassic alteration), quartz-sericite (phyllic alteration), tourmaline, and specularite (Fig. 6). Mineral zonation also has been summarized schematically in section XC 50ss, based on detailed drill core logging and thin section petrography, and supplemented by data from the mine's digital database (Fig. 3).

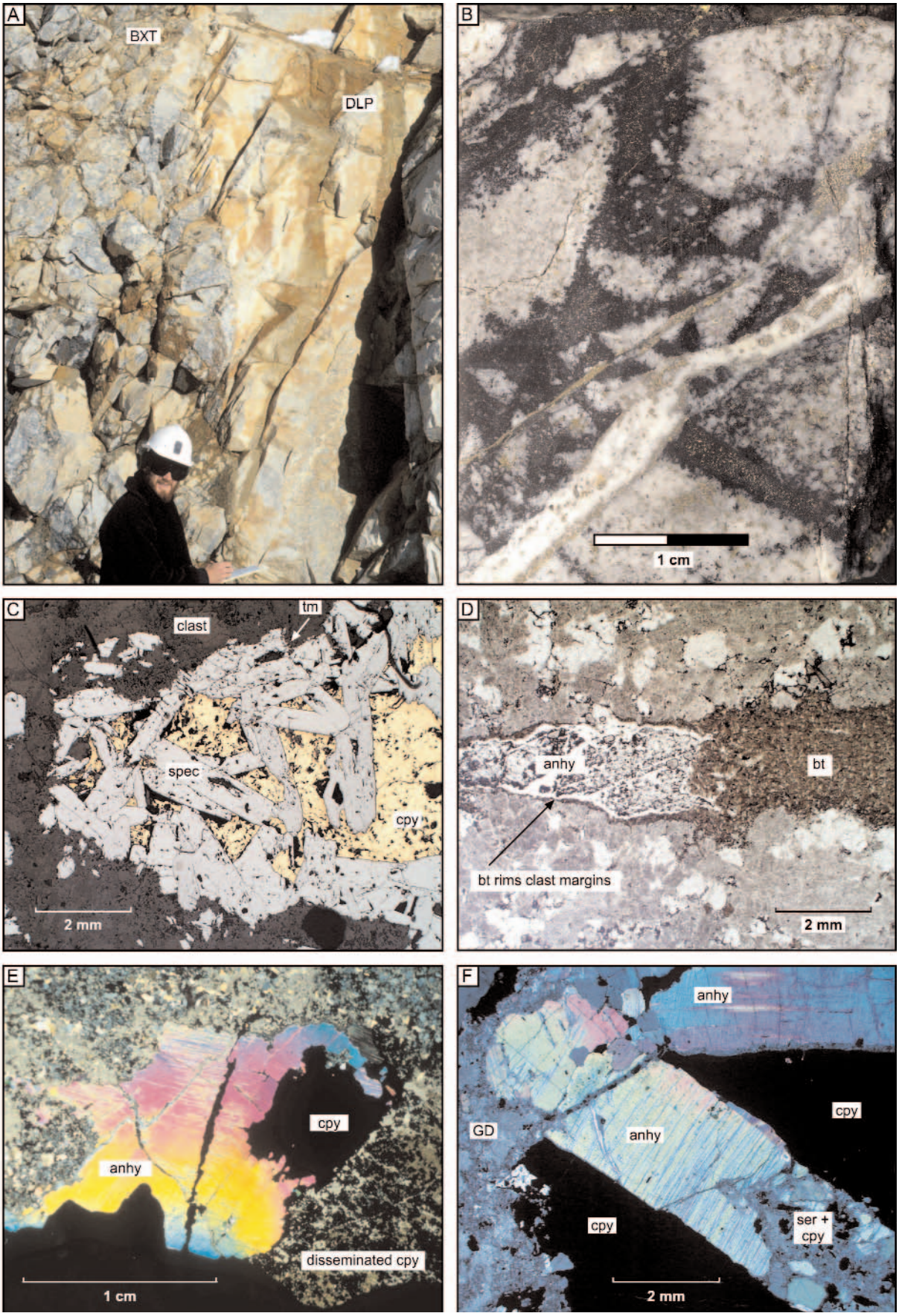
A
BXT
DLP
B
1 cm
C
clast
tm
spec
cpy
2 mm
D
anhy
bt
bt rims clast margins
2 mm
E
cpy
anhy
disseminated cpy
1 cm
F
anhy
cpy
GD
anhy
cpy
ser + cpy
2 mm

A well-defined mineral and alteration zonation from north to south in the tourmaline breccia body along section D-D' (Fig. 6) correlates with the zonation observed at Sur-Sur in section XC 50ss (Fig. 3). Biotite-cemented breccias associated with potassic alteration occur in the Don Luis sector and deep in the Sur-Sur sector (Figs. 3, 6A). The biotite-cemented breccias in the Don Luis sector have elevated hypogene copper grades (0.75–1% Cu); however, the biotite breccia at the base of the Sur-Sur tourmaline breccia has low copper grades (0.2–0.3% Cu). Above and to the south of the potassic alteration zone, a transitional zone of approximately 100 m in the vertical rock column separates biotite (potassic) alteration and quartz-sericite (phyllic) alteration (Fig. 3). Textural relationships between hydrothermal biotite and tourmaline in the transitional zone are unclear due to the fine-grained nature of these minerals.

The distribution of quartz-sericite (phyllic) alteration correlates with the distribution of tourmaline cement in the Don Luis, Sur-Sur, and La Americana sectors (Figs. 3, 6B, C). The tourmaline-cemented breccias and phyllic alteration assemblage are also associated with elevated hypogene copper grades (~1% Cu). High-grade ore in the Don Luis and Río Blanco sectors is associated with biotite alteration and cementation.

The findings of Vargas et al. (1999) are confirmed by the specularite distribution shown in Figures 3 and 6D. Most specularite occurs above and to the sides of the Sur-Sur and Don Luis mineralized centers (Figs. 3, 6D).

Ar-Ar Geochronology

Deckart et al. (2005) provides comprehensive new U-Pb and Ar-Ar datasets for Río Blanco-Los Bronces, together with a detailed appraisal of the magmatic-hydrothermal evolution of the ore deposit. We supplement this data set with two Ar-Ar analyses to help determine the timing of biotite and tourmaline cementation.

Previous geochronological studies on the Sur-Sur tourmaline breccia have been performed on altered whole-rock breccia samples (e.g., Warnaars et al., 1985; Serrano et al., 1996). They yielded ages of 7.1 ± 0.8 and 5.1 ± 0.2 Ma (Table 1; Serrano et al., 1996). The Río Blanco magmatic breccia has been dated previously using both whole-rock samples and mineral separates (biotite, K-feldspar), which gave ages between 7.3 ± 0.7 and 4.2 ± 0.1 Ma (Serrano et al., 1996). In both cases, the older ages were obtained from whole-rock samples using the K-Ar technique; whereas younger ages were obtained from pure mineral separates of biotite and K-feldspar using the $^{40}Ar/^{39}Ar$ technique.

In this study, hydrothermal (secondary) biotite was handpicked from a sample of fine-grained cement collected from the deepest levels of the Sur-Sur tourmaline breccia (2,873-m elevation). In addition, pervasive sericite-altered granodiorite clasts were collected from a high-level tourmaline breccia sample (4,021-m elevation). The altered clasts were separated from the tourmaline cement and powdered prior to analysis. Sample locations, elevations, and results for the Ar-Ar study are listed in Table 1, and stepwise release spectra are illustrated in Figure 7. The plateau age for hydrothermal biotite is 4.78 ± 0.04 Ma. This age is similar to, but does not overlap with, $^{40}Ar/^{39}Ar$ age determinations for biotite (4.6 ± 0.1 Ma) and K-feldspar (4.2 ± 0.1 Ma) from the magmatic breccia in the Río Blanco sector (Serrano et al., 1996). The plateau age for the sericite-altered whole-rock sample is 5.42 ± 0.09 Ma and is similar to the whole-rock ages reported previously for the tourmaline breccia (Serrano et al., 1996).

As discussed in Deckart et al. (2005), the ore deposit has been the site of repeated and widespread postmineralization intrusive activity that could have reset Ar-Ar and K-Ar isotope systems. The age of our shallow-level sericite-altered breccia sample (5.42 ± 0.09 Ma) is notably older than the biotite cement (4.78 ± 0.04 Ma); even though textural relationships in the breccia indicate that the biotite and sericite probably formed contemporaneously. The discrepancy in Ar-Ar ages is therefore best explained by isotopic resetting, with the shallow-level sericite sample cooling below the Ar-Ar closure temperature approximately 600,000 yr prior to the biotite sample from approximately 1,250 m deeper within the ore deposit.

Observed crosscutting relationships (Frikken, 2004) show that the magmatic breccia at Río Blanco predates the intrusion of the quartz monzonite porphyry (U-Pb age: 6.32 ± 0.09 Ma) and that the tourmaline breccia at Sur-Sur predates the emplacement of the feldspar porphyry dike (U-Pb age: 5.84 ± 0.03 Ma). Therefore, these intrusions provide minimum age constraints on the mineralized breccias at Río Blanco-Los Bronces.

FIG. 4. Photographs and photomicrographs of rocks and ores from the Sur-Sur tourmaline breccia. A. Subvertical intrusive contact between the Sur-Sur tourmaline breccia (BXT) and the postmineral Don Luis porphyry (DLP). B. Hand specimen of mineralized tourmaline breccia from the Sur-Sur open pit. Angular clasts of granodiorite have been pervasively altered to quartz-sericite-pyrite-chalcopyrite. Tourmaline occurs as an alteration selvage on clast margins and has grown both into and outward from clast margins. Voids between tourmaline needles have been filled by chalcopyrite. The breccia cement and clasts are cut by a late-stage, 1-cm-wide vuggy quartz-chalcopyrite-pyrite vein and a thin (1-mm) pyrite-chalcopyrite vein. Scale in centimeters. C. Photomicrograph of oxide-stage specularite that has grown into space from a thin selvage of tourmaline at clast margins and has been overgrown by chalcopyrite. Note that specularite is stable in the presence of chalcopyrite and no magnetite is present (sample 492, DL-57, 4,021 m asl; reflected light). D. Photomicrograph of biotite breccia from the deepest intersections of the Sur-Sur breccia complex. Biotite occurs as rims around clast margins and as infill. Anhydrite has partially cemented the central void space (sample 215a, TSS-22, 2,873 m asl; transmitted light). E. Photomicrograph of anhydrite cement replaced by chalcopyrite. The chalcopyrite has penetrated cleavage planes in the anhydrite crystal and also occurs in two fractures that cut the anhydrite grain (sample 335, DDH-628, 3,261 m asl; transmitted light). F. Photomicrograph of an anhydrite crystal cut by chalcopyrite and sericite (breccia cement mineralization stage, transmitted light). Abbreviations: anhy = anhydrite, bt = biotite, cpy = chalcopyrite, GD = granodiorite, ser = sericite, spec = specularite, tm = tourmaline.

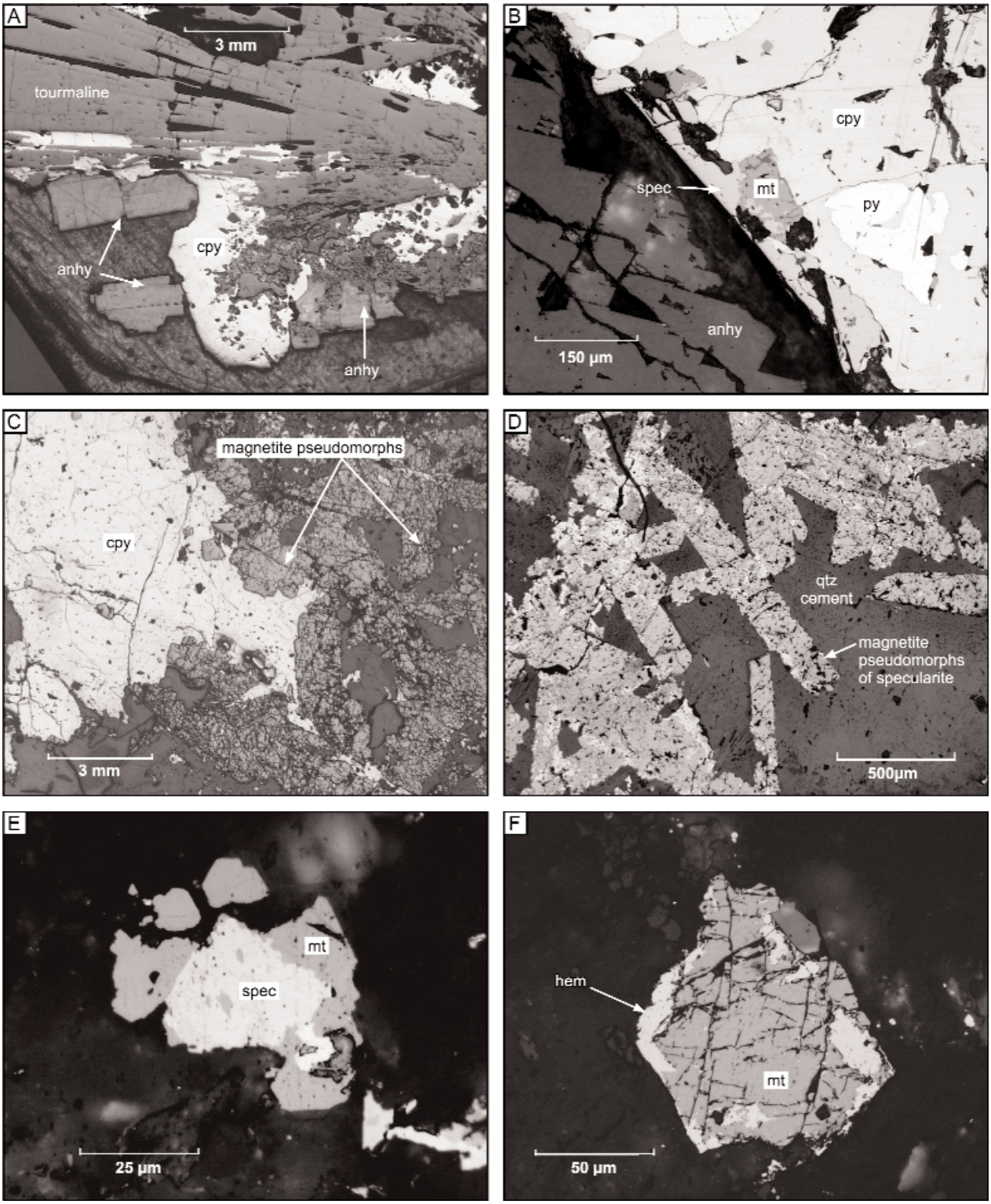

FIG. 5. Reflected light photomicrographs of Sur-Sur tourmaline breccia. A. Early tourmaline and anhydrite crystals cut and partially replaced by chalcopyrite (sample 62b, TSS-22, 2,919 m asl). B. Photomicrograph showing specularite in contact with anhydrite and chalcopyrite. The specularite has been partially replaced by magnetite. Chalcopyrite contains pyrite inclusions (sample 01BXT12, TSS-12, 3,541 m asl). C. In this sample, magnetite associated with the mineralization event forms an almost complete pseudomorph of oxide-stage specularite (sample 523, DL-71, 4,033 m asl). D. Magnetite pseudomorphs after specularite. Magnetite crystals have been partially replaced at their outer margins and along internal fractures by late-stage hematite (sample 523, DL-71, 4,033 m asl). E. Early specularite replaced by magnetite (sample 7, TSS-4, 3,708 m asl). F. Late-stage hematite alteration of magnetite associated with a postbreccia vein (sample 01BXT12, TSS-12, 3,541 m asl). Abbreviations: anhy = anhydrite, cpy = chalcopyrite, hem = hematite, mt = magnetite, py = pyrite, qz = quartz, spec = specularite.

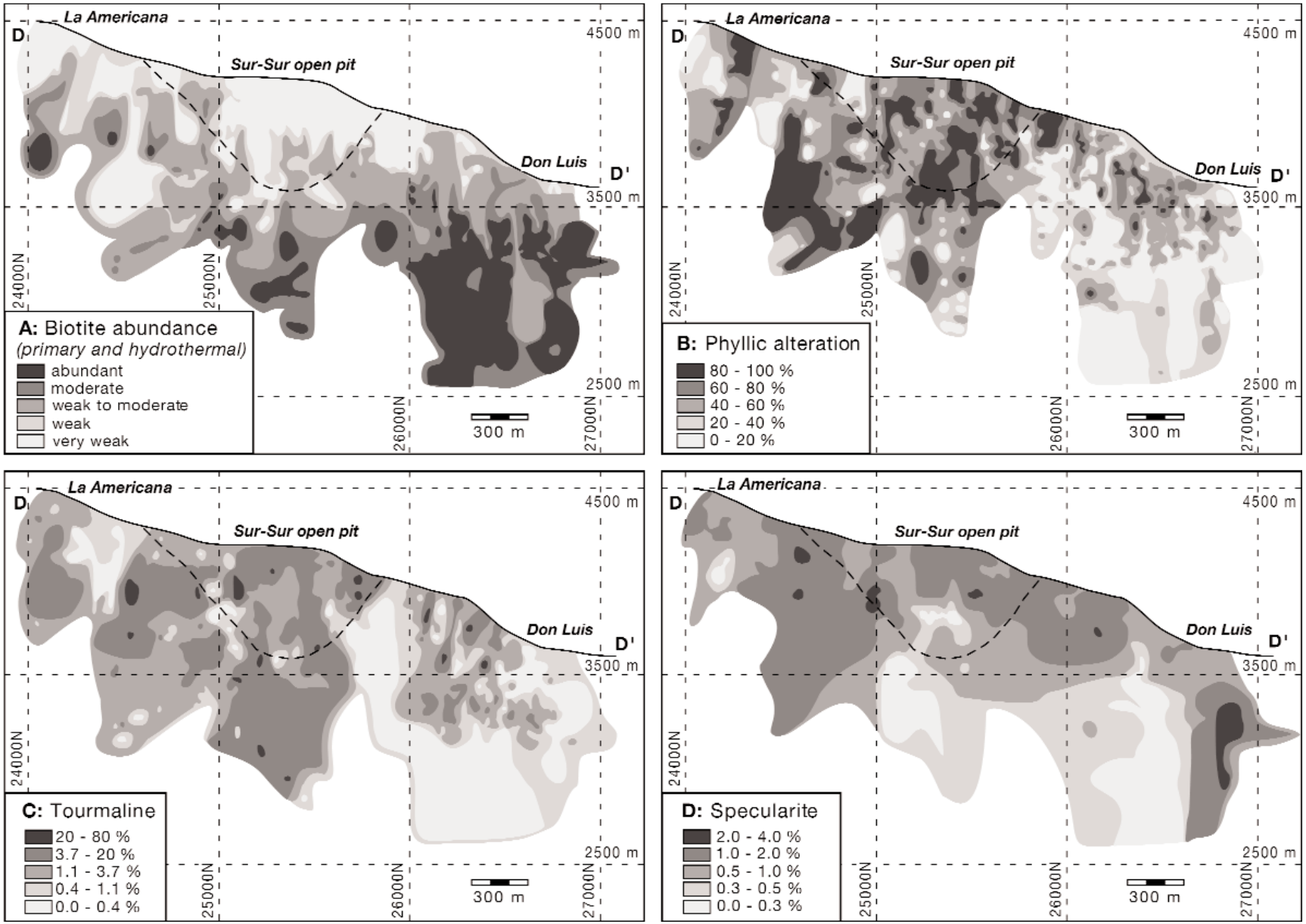

FIG. 6. Mineralogical distribution in longitudinal section D-D' through the Sur-Sur tourmaline breccia. The location of the section is shown in Figure 1. Note that the mineral abundances are qualitative estimates made by CODELCO geologists during drill core logging. A. Biotite. Both primary and hydrothermal biotite is shown in this section, as the CODELCO digital database does not discriminate between these two types. (Abundant: biotite alteration widespread and pervasively developed within a 1-m core intersection, easily visible to the naked eye; Moderate: biotite present as a selectively pervasive alteration mineral, an obvious vein halo alteration mineral, or as primary disseminations; Weak to very weak: biotite observed rarely with naked eye or hand lens). B. Visual estimate of the abundance of phyllic alteration (defined by secondary quartz-sericite) plotted as volume percent for each 1-m core intersection. C. Tourmaline (visual estimate; vol %). D. Specularite (visual estimate; vol. %).

TABLE 1. Step-heating ^{40}Ar-^{39}Ar Isotope Data, Apparent Ages, and Plateau Ages for Hydrothermal Biotite Cement (sample 215a; 2,873-m elev) and Sericite Whole Rock (sample 530; 4,021-m elev)

Sample 215a - mass = 0.9 mg, J value = 0.002451 ± 0.000018

DDH	Section	Meters	Altitude	Lithology	Material	Method	^{39}Ar released	Plateau age (Ma)
TSS 22	XC-50	782 m	2,873 m	BXMGD	Hydrothermal biotite	Ar/Ar	86%	4.78 ± 0.04 Ma

Power	$^{36}Ar/^{40}Ar$	$^{39}Ar/^{40}Ar$	r	Ca/K	% 40Atm	% ^{39}Ar	$^{39}Ar/^{40}Ar^*$	Age
0.5	0.0034	0.0343	0.049	0.697	100.53	0.14	–0.183	–0.81± 5.44
1	0.0031	0.1786	0.243	0.392	91.74	0.48	0.435	1.92 ± 1.64
1.5	0.0015	0.5174	0.068	0.21	44.62	2.44	1.057	4.67 ± 0.29
1.75	0.0006	0.7598	0.007	0.065	17.69	6.65	1.078	4.76 ± 0.12
2	0.0004	0.8335	0.009	0.044	12.74	4.81	1.043	4.61 ± 0.10
<2.25>	0.0003	0.8314	0.002	0.078	10.41	3.77	1.074	4.74 ± 0.16
<2.75>	0.0004	0.8155	0.002	0.109	11.42	4.14	1.083	4.78 ± 0.16
<3.50>	0.0003	0.8154	0.006	0.27	11.22	4.93	1.085	4.79 ± 0.11
<4.50>	0.0002	0.8551	0.002	0.406	6.37	6.4	1.093	4.83 ± 0.08
<7.00>	0.0001	0.8796	0.013	0.268	4.62	66.22	1.083	4.78 ± 0.02

Volume ^{39}K: 61.53 × 1E-10 cm^3 NTP
Integrated age: 4.75 ± 0.04 Ma
Initial $^{40}Ar/^{36}Ar$: 320.54 ± 98.19 (MSWD = 0.55, isochron between 0.18 and 2.63)
Correlation age: 4.76 ± 0.09 Ma (85.5% of ^{39}Ar, steps marked by >)
Plateau age: 4.78 ± 0.04 Ma (85.5% of ^{39}Ar, steps marked by <)
All errors are 2 × standard error

Sample 530 - mass = 0.9 mg, J value = 0.002449 ± 0.000018

DDH	Section	Meters	Altitude	Lithology	Material	Method	^{39}Ar released	Plateau age
DL-53	XC-30	50 m	4,021 m	BXT	WR sericite	Ar/Ar	81%	5.42 ± 0.09 Ma

Power	$^{36}Ar/^{40}Ar$	$^{39}Ar/^{40}Ar$	r	Ca/K	% 40Atm	% ^{39}Ar	$^{39}Ar/^{40}Ar^*$	Age
0.5>	0.0034	0.0003	0.151	0.064	102.01	0.46	–54.75	–259.73 ± 213.55
0.75>	0.0033	0.0016	0.013	0.033	99.45	0.55	3.421	15.05 ± 38.88
1>	0.0033	0.0065	0.003	0.012	99.32	0.87	1.003	4.42 ± 9.54
1.25>	0.0032	0.0229	0.005	0.005	96.85	1.24	1.348	5.94 ± 3.05
1.5>	0.0031	0.0621	0.007	0.005	91.76	1.76	1.297	5.72 ± 1.42
1.75>	0.0025	0.1915	0.011	0.003	74.93	3.31	1.286	5.67 ± 0.44
2.25>	0.0026	0.1559	0.01	0.003	78.61	4.12	1.348	5.95 ± 0.48
<2.75>	0.0026	0.1649	0.009	0.003	79.07	6.71	1.245	5.49 ± 0.39
<3.25>	0.0023	0.257	0.007	0.004	68.01	9.24	1.224	5.40 ± 0.25
<3.75>	0.0022	0.2836	0.008	0.004	64.95	13.05	1.216	5.37 ± 0.19
<4.25>	0.0021	0.3042	0.012	0.003	62.11	17.2	1.227	5.41 ± 0.16
<4.75>	0.0016	0.4062	0.012	0.004	49.34	14.54	1.232	5.44 ± 0.13
<5.50>	0.0018	0.3746	0.008	0.008	53.43	12.28	1.227	5.41 ± 0.15
<6.50>	0.0016	0.4168	0.01	0.01	48.01	7.83	1.233	5.44 ± 0.16
7	0.0025	0.1847	0.014	0.053	73.96	6.86	1.387	6.12 ± 0.37

Volume ^{39}K: 43.51 × 1E-10 cm^3 NTP
Integrated age: 4.42 ± 0.91 Ma
Initial $^{40}Ar/^{36}Ar$: 295.17 ± 6.8 (MSWD = 1.23, isochron between 0.59 and 1.82)
Correlation age: 5.43 ± 0.08 Ma (93.1% of ^{39}Ar, steps marked by >)
Plateau age: 5.42 ± 0.09 Ma (80.8% of ^{39}Ar, steps marked by <)
All errors are 2 × standard error

Sulfur Isotope Geochemistry

Sulfur isotope compositions of sulfides from Sur-Sur have been determined using conventional techniques to separate coarse-grained sulfides (Robinson and Kusakabe, 1975) and by the laser-ablation method for fine-grained (100–300 μm) sulfides (Huston et al., 1993). Laser-ablation analysis of sulfur isotopes was performed using a 117 Nd:YAG laser. The analytical uncertainty for the conventional technique is estimated to be ±0.2 per mil. An analytical uncertainty of ±0.1 per mil is estimated from internal standards of homogenous galena from Broken Hill ($\delta^{34}S$ = 3.4‰) and Rosebery ($\delta^{34}S$ = 12.4‰) run with an SO_2 reference gas of $\delta^{34}S \approx$ CDT. These internal standards were calibrated against international sphalerite standards IAEA NZ1 ($\delta^{34}S$ = 1.83‰) and NBS ($\delta^{34}S$ = 4.34‰).

One hundred and fourteen sulfur isotope analyses were completed in the current study on sulfides from three mineralized paragenetic stages identified in the Sur-Sur sector: (1) sulfide cement (n = 72), (2) postbreccia quartz sulfide veins

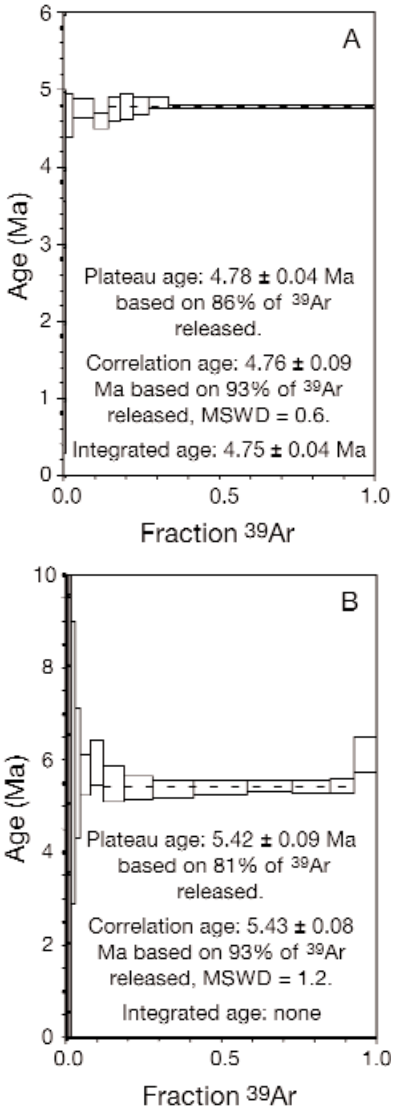

FIG. 7. $^{40}Ar/^{39}Ar$ apparent age spectra for (A) hydrothermal biotite and (B) sericite-altered whole-rock samples from the Sur-Sur tourmaline breccia.

(n = 27), and (3) late-stage pyrite-rich veins (n = 15; Table 2, Fig. 8). In addition, seven sulfur isotope analyses were obtained from anhydrite cement in the tourmaline breccia (Table 2). All data for section XC 50ss are shown in Figure 9,

TABLE 2. Summary Statistics for Sulfur Isotope Analyses of Sulfides and Sulfates from Sur-Sur

Mineral	n	Mean $\delta^{34}S$ ‰	Range $\delta^{34}S$ ‰	Standard deviation
Sulfide cement	72	–1.1	–4.1 to +2.7	1.5
Sulfide veins (qtz/ser)	27	–0.9	–4.1 to +2.5	1.2
Late stage pyrite-rich veins	15	–0.4	–1.7 to +1.1	0.8
Sulfides (Total)	114	–0.8	–4.1 to +2.7	1.4
Sulfate cement	7	+12.2	+11.2 to +13.4	0.9

Abbreviations: qtz = quartz, ser = sericite

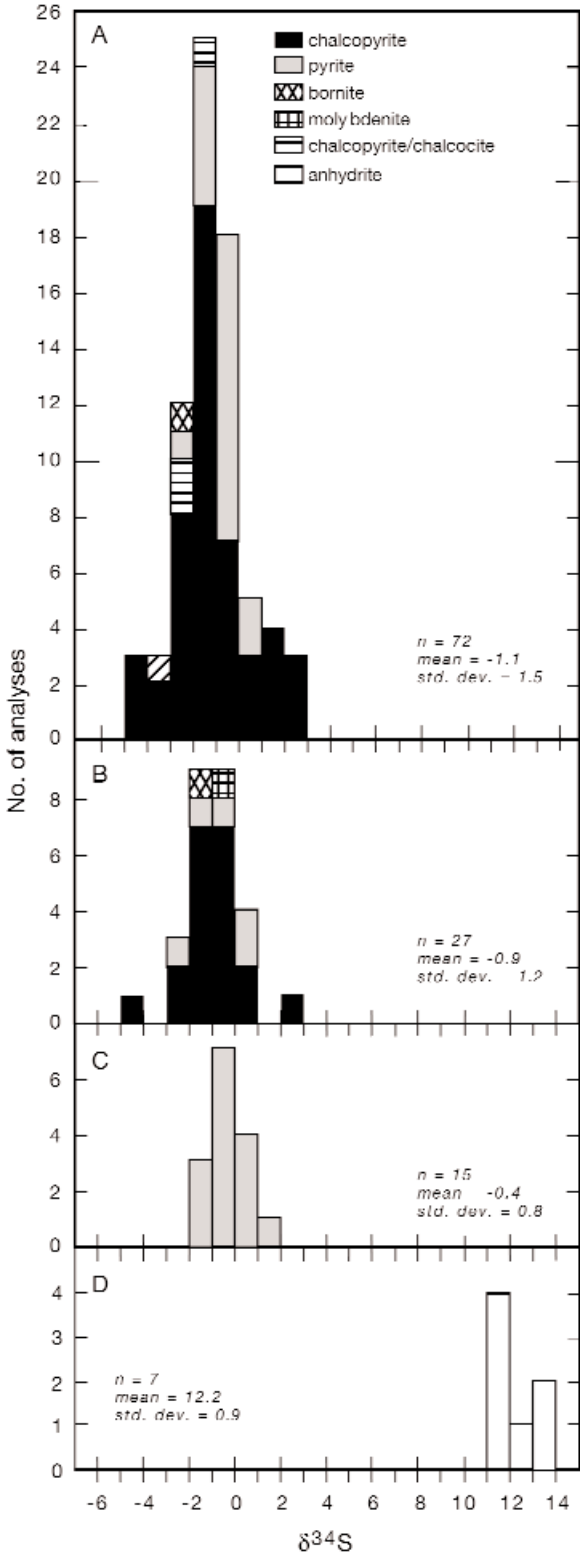

FIG. 8. Histograms of sulfur isotope data from the Sur-Sur tourmaline breccia in paragenetic order. A. Tourmaline breccia sulfide cement. B. Sulfide veins with associated quartz-sericite alteration halos. C. Late-stage pyrite-rich veins. D. Tourmaline breccia anhydrite cement. The late-stage pyrite-rich veins have sulfur isotope compositions clustered around zero per mil, whereas many of the sulfides in the breccia cement and sulfide veins with quartz-sericite halos have negative sulfur isotope compositions, probably due to deposition from an oxidizing magmatic-hydrothermal fluid.

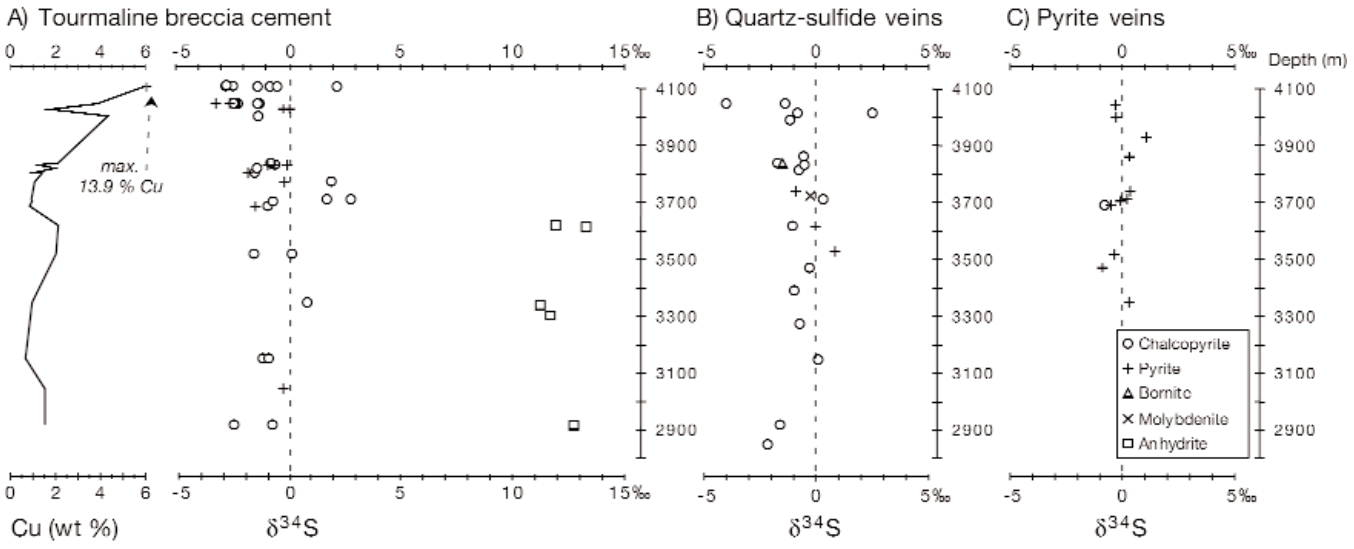

FIG. 9. Copper grades and sulfur isotope compositions of (A) sulfide and sulfate cement from the tourmaline breccia, (B) postbreccia quartz sulfide veins, and (C) pyrite-rich veins, plotted as a function of depth. All samples were collected from section XC 50ss in Sur-Sur sector. Copper grades relate only to the tourmaline breccia cement. The highest copper grades correlate with the lowest $\delta^{34}S$ values obtained for sulfide breccia cement from the top of the Sur-Sur tourmaline breccia.

and the complete data set for Sur-Sur is available as a digital supplement to this paper at <www.segweb.org/EG/papers/Abs100-5_files/07FrikkenAppendix.pdf>.

Tourmaline breccia-sulfide cement

Sulfur isotope compositions were determined on chalcopyrite (n = 48), pyrite (n = 20), bornite (n = 1), and chalcopyrite and/or chalcocite composites (n = 3). Results range from –4.1 to +2.7 per mil with a mean value of –1.1 per mil (Table 2).

Sulfur isotope compositions of sulfide cement of the tourmaline breccia are zoned spatially (Figs. 10A, 11). Samples located at the highest altitudes in the tourmaline breccia (>4,000 m asl) have the lowest $\delta^{34}S$ sulfide values (Figs. 9, 10A), coincident with the high-grade zone at Sur-Sur (Fig. 10B). Similarly low values occur both to the north and south, along strike of the Sur-Sur tourmaline breccia body and in the deepest drill hole in section XC 50ss (Fig. 11). Chalcopyrite has been partly replaced by supergene chalcocite at these elevations, but laser-ablation analyses of coexisting chalcopyrite and chalcocite grains indicate no significant difference in sulfur isotope compositions compared to those obtained from composite grains (Fig. 8A, App. 1). Therefore, the low $\delta^{34}S$ values at the top of the breccia body are not a function of supergene effects.

As for chalcopyrite, the lowest $\delta^{34}S$ values in pyrite were obtained above 4,000-m elevation (Fig. 9). These results indicate that sulfide sulfur was fractionated to progressively lower values upward through the breccia column during hypogene sulfide deposition.

Tourmaline breccia-sulfate cement

Sulfur isotope results from seven anhydrite samples from the tourmaline breccia cement have $\delta^{34}S$ values between 11.2 and 13.4 per mil, with a mean value of 12.2 per mil (Table 2, Fig. 8D). Anhydrite occurs below the incipiently weathered zone at 3,600-m elevation in Sur-Sur (Fig. 3). Above this zone, gypsum is the only sulfate mineral present. The narrow range of values suggests no significant fractionation of sulfur isotopes during anhydrite deposition in the lower parts of the Sur-Sur tourmaline breccia, although only a limited number of samples were analyzed.

Postbreccia quartz sulfide veins

Sulfur isotope compositions were determined for 27 sulfides from chalcopyrite + pyrite-bearing quartz veins with quartz-sericite alteration halos that cut the tourmaline breccia at Sur-Sur. Analyses were performed on chalcopyrite (n = 20), pyrite (n = 5), bornite (n = 1), and molybdenite (n = 1), and results range between –4.1 and +2.5 per mil, with a mean value of –0.9 (Fig. 8B; Table 2). The lowest values were obtained from the top of the Sur-Sur tourmaline breccia body, as in the breccia cement.

Pyrite veins

Sulfur isotope compositions of 15 pyrite samples from late-stage pyrite-rich veins range between –1.7 and +1.1 per mil, with a mean value of –0.4 per mil (Table 2). The lowest values are located to the north and south, along strike of the tourmaline breccia body and outside the main mineralized system. Although these veins contain gypsum and traces of anhydrite and chalcopyrite in addition to abundant pyrite, the low abundances of anhydrite and chalcopyrite prevented analyses of any mineral pairs. Sulfides analyzed from the late-stage pyrite veins do not vary significantly from 0 per mil (Fig. 8C; Table 2), indicating limited sulfur isotope fractionation within the hydrothermal fluid during this stage.

Fluid Inclusions

We have performed a total of 328 microthermometric analyses on fluid inclusions in quartz (305 from 15 samples) and tourmaline cement (23 from five samples) from the Sur-Sur tourmaline breccia (Appendix 2). These samples were selected to provide maximum spatial coverage and

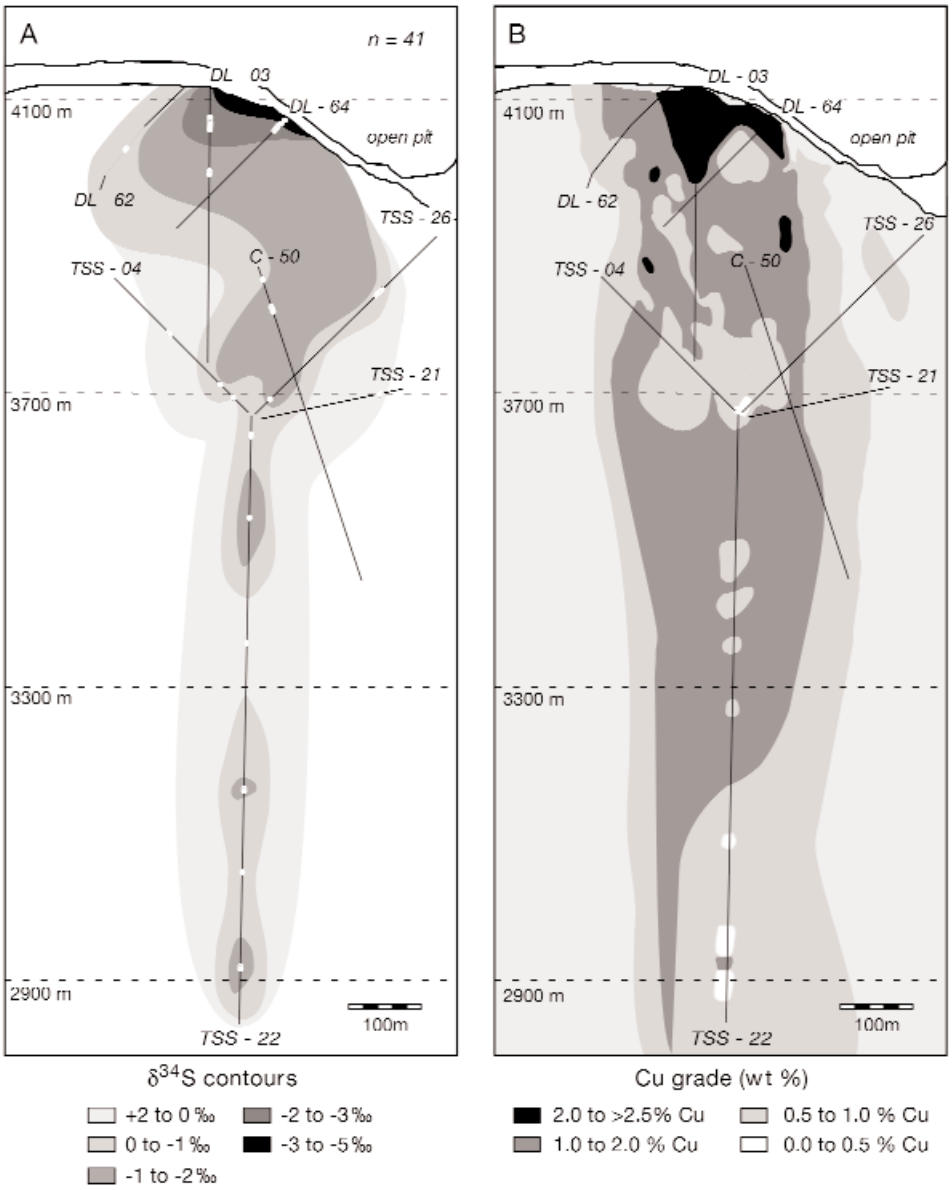

FIG. 10. A. Spatial zonation of sulfur isotope compositions of sulfide cement in section XC 50ss. Open circles represents sample locations. B. Copper-grade distribution in section XC 50ss. The location of the section is shown in Figure 1. The highest copper grades correlate with sulfide minerals that have the lowest analyzed sulfur isotope compositions from the Sur-Sur breccia.

also to provide temperature constraints on the sulfur isotope data set. Note that in this and subsequent discussions, fluids with salinities of <10 wt percent NaCl are referred to as low salinity aqueous liquids, saline aqueous liquids (>10 wt % NaCl) are referred to as brines, and salt-saturated liquids at room temperature are referred to as hypersaline liquids.

Microthermometric measurements were performed at the University of Tasmania using a Linkam MDS600 heating-freezing stage manufactured by Linkam Scientific Instruments Ltd. The Linkam stage has an upper temperature limit of 600ºC and was calibrated using synthetic fluid inclusions supplied by Synflinc Inc. The precision of measured temperatures is ±1.0ºC for heating and ±0.3ºC for freezing (Rae et al., 2003). Salinities were calculated as wt percent NaCl equiv or, in the case of hypersaline fluid inclusions that contain halite and sylvite daughter crystals, wt percent NaCl + KCl equiv. The salinity of halite-undersaturated inclusions was calculated from measured freezing point depression temperatures by applying a linear least squares regression (Potter et al., 1978). The salinity of halite-saturated inclusions was calculated from halite dissolution temperatures using the SALTY algorithm (Bodnar et al., 1989).

Fluid inclusions have been classified based on observed phase relationships at room temperature (Figs. 12, 13). Type i are two- or three-phase, liquid-rich fluid inclusions that homogenize to liquid on heating. They are subdivided into type ia (liquid + vapor) and ib (liquid + vapor + opaque; Fig. 12). Type ii are salt-saturated (halite- and/or sylvite-bearing) fluid

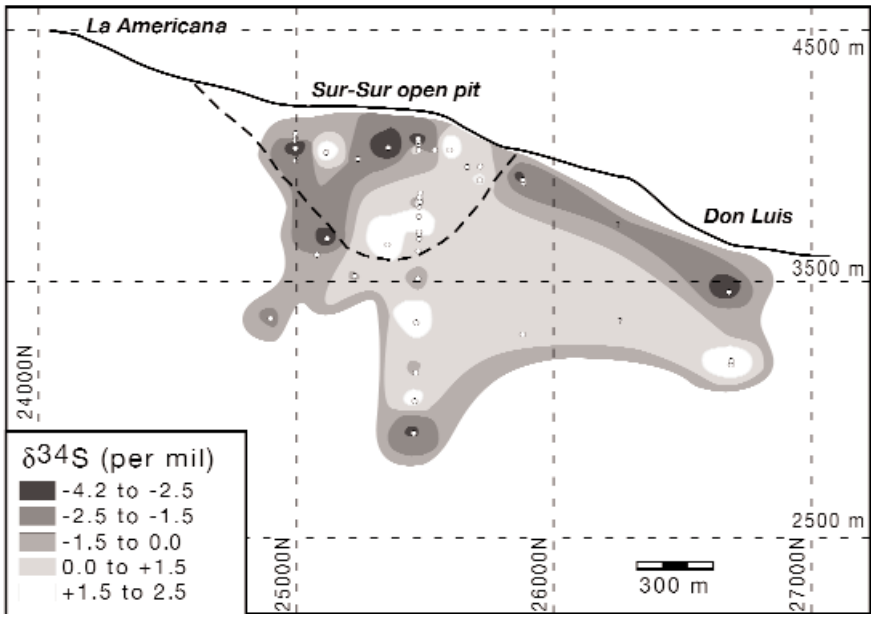

FIG. 11. Spatial zonation of sulfur isotope compositions of sulfide cement in longitudinal section D-D' through the Sur-Sur tourmaline breccia. Open circles represent sample locations. The location of the section is shown in Figure 1. The lowest $\delta^{34}S$ values obtained from sulfides in the Sur-Sur tourmaline breccia occur in the two mining sectors of Sur-Sur and Don Luis.

Inclusion type	Phases at 25°C	Homogenization behavior
Type i		
a 	Liquid > vapor	Vapor disappears
b 	Liquid > vapor + opaque	Vapor disappears, solid phase does not dissolve on heating
Type ii		
a 	Liquid-vapor-halite	Vapor + halite disappear
b 	Liquid-vapor-sylvite	Vapor + sylvite disappear
c 	Liquid-vapor-halite-sylvite hematite-anhydrite-opaque	Vapor + halite + sylvite + anhydrite disappear, non-soluble solids remain upon heating
Type iii		
	Vapor > liquid	Liquid disappears

FIG. 12. Fluid inclusion types recognized in quartz and tourmaline cement from the Sur-Sur breccia. Based on petrographic observations made at room temperature, six types of fluid inclusions were recognized. Type ia are two-phase (liquid + vapor), undersaturated liquid-rich fluid inclusions that homogenize to a liquid. Type ib are three-phase (liquid + vapor + insoluble solid), undersaturated liquid-rich fluid inclusions that contain an unknown insoluble opaque mineral. These inclusions homogenize to a liquid, but the solid phases do not dissolve. Type iia are three-phase hypersaline inclusions with a halite daughter salt and vapor bubble in a liquid. These inclusions homogenize either by vapor disappearance or halite dissolution. Type iib are three-phase hypersaline inclusions with a sylvite daughter salt and vapor bubble in a liquid. Type iic are multiphase (at least four phases) hypersaline inclusions with a variety of daughter minerals present in addition to vapor and liquid. These may include halite, sylvite, anhydrite, hematite, and/or opaque. Type iii are two-phase (vapor + liquid) undersaturated vapor-rich inclusions that either homogenize to vapor or decrepitate before homogenization.

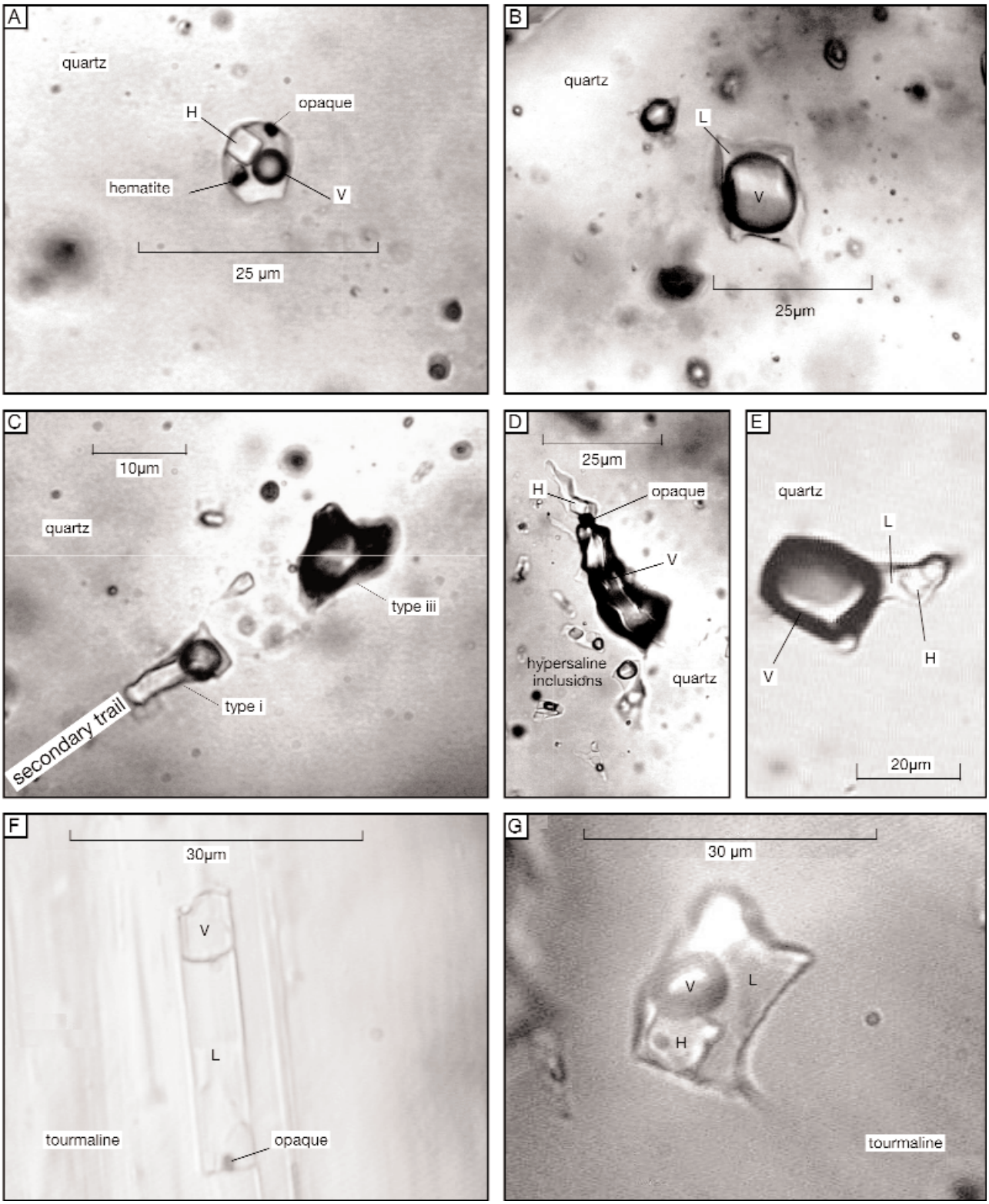

FIG. 13. Photomicrographs of fluid inclusions in quartz and tourmaline cement from the Sur-Sur breccia. A. Type iic = halite, hematite, opaque, and vapor-bearing polyphase hypersaline fluid inclusions in quartz. B. Type iii = vapor-rich inclusions in quartz. C. Type ia = secondary trail containing coexisting type i, liquid-rich and type iii, vapor-rich fluid inclusions in quartz (sample 190). D. Coexisting type ii, hypersaline and type iii, vapor-rich fluid inclusions; the vapor-rich inclusion also contains a halite daughter crystal and an opaque in quartz (sample 490). E. A hybrid vapor-rich inclusion that also contains a halite daughter crystal. T_h (halite) = 527°C, T_h (vapor) = >600°C in quartz (sample 524). F. Type ib = liquid-rich inclusion with an opaque in tourmaline. G. Type iia = halite and vapor hypersaline inclusion in tourmaline. Abbreviations: H = halite, L = liquid, V = vapor.

inclusions that have been subdivided into type iia (liquid + vapor + halite), iib (liquid + vapor + sylvite), and iic (liquid + vapor + several daughter minerals; Fig. 12). Type ii inclusions homogenize by vapor bubble disappearance or salt dissolution. Type iii are vapor-rich fluid inclusions that homogenize to the vapor phase. The fluid inclusions range in maximum dimension up to 40μm but those analyzed were typically between 10- and 20-μm diameter. Based on the criteria of Roedder (1984), unequivocal evidence of primary origins for fluid inclusions was not observed, and all inclusions were assumed to be secondary. Our complete fluid inclusion data set is available as a digital supplement to this paper at www.segweb.org/EG/papers/Abs100-5_files/07FrikkenAppendix.pdf.

The three major types of fluid inclusions summarized in Figure 12 were observed only in quartz cement from the tourmaline breccia. Tourmaline does not contain any vapor-rich fluid inclusions, although rare type ia, ib, and iic fluid inclusions were observed along cleavage planes (Fig. 12). Although we have not analyzed fluid inclusions in anhydrite from Sur-Sur, Frikken (2004) analyzed salt-undersaturated (types i and iii) fluid inclusions from anhydrite cement in biotite-cemented breccia in the Río Blanco sector.

Quartz-hosted fluid inclusions

The fluid inclusions analyzed in quartz cement from the tourmaline breccia were type ia (n = 100), type ib (n = 2), type iia (n = 152), type iib (n = 2), type iic (n = 23), and type iii (n = 26; Figs. 14, 15). Most of the samples were collected from section XC 50ss (Fig. 16). Individual samples were also collected from sections XC-00ss, XC-40ss, and XC-70ss (located 220 and 44 m to the north and 88 m to the south of XC 50ss, respectively), in order to obtain greater spatial coverage of data (Fig. 1). The samples were collected at elevations from 2,919 to 4,066 m. Type iii fluid inclusions are most common, comprising 50 percent of all inclusions present. Generally, types i and ii inclusions are smaller (5–15μm) than coexisting type iii inclusions (10–20μm). Daughter minerals in type ii fluid inclusions include halite, sylvite, opaque, anhydrite, tourmaline, and hematite (Fig. 12).

Measured vapor homogenization temperatures (T_hV) for type i fluid inclusions range widely (195°–446°C), with most between 300° and 440°C (Table 3, Fig. 14A). Vapor homogenization temperatures for type ii fluid inclusions range from 135° to >600°C. Liquid homogenization temperatures (T_hL) for type iii fluid inclusions range from 353° to >600°C (Table

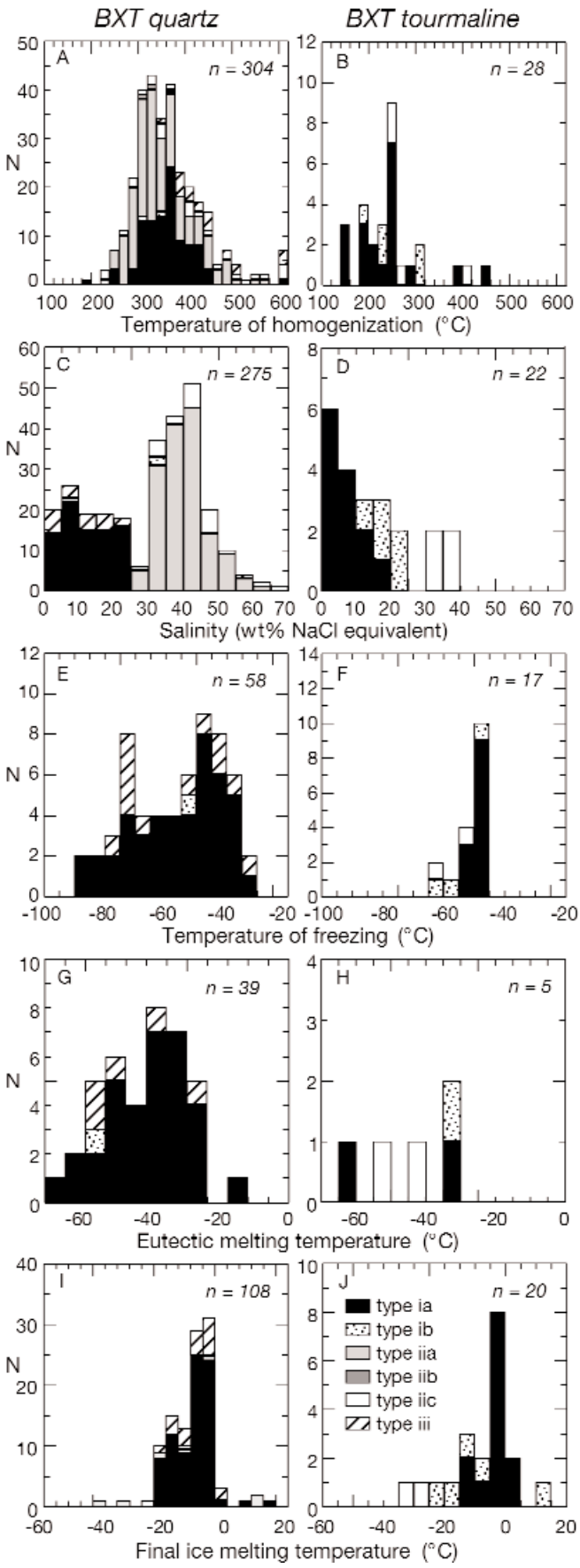

FIG. 14. Frequency histograms of (A, B) homogenization temperatures (T_h), (C, D) salinities (wt % NaCl equiv), (E, F) freezing temperatures (T_f), (G, H) eutectic temperatures (T_e) and (I, J) final melting temperatures (T_m) for quartz and tourmaline cement (F-J) in the Sur-Sur mineralized system. BXT quartz = quartz cement (tourmaline breccia), BXT tourmaline = tourmaline cement (tourmaline breccia). Similar ranges of temperatures and salinities have been obtained for the different fluid inclusion types. Note, however, that hypersaline fluid inclusions were not analyzed from tourmaline, although they were observed rarely (e.g., Fig. 13G). Many of the eutectic melting temperatures are lower than –35ºC, suggesting the presence of abundant divalent cations such as Ca or Fe in addition to Na and K in solution. This has been confirmed by proton-induced X-ray emission (PIXE) analyses of nine fluid inclusions from Sur-Sur, with maximum concentrations of 0.89 wt percent Ca and 0.64 wt percent Fe detected during analyses of nine fluid inclusions (Frikken, 2004).

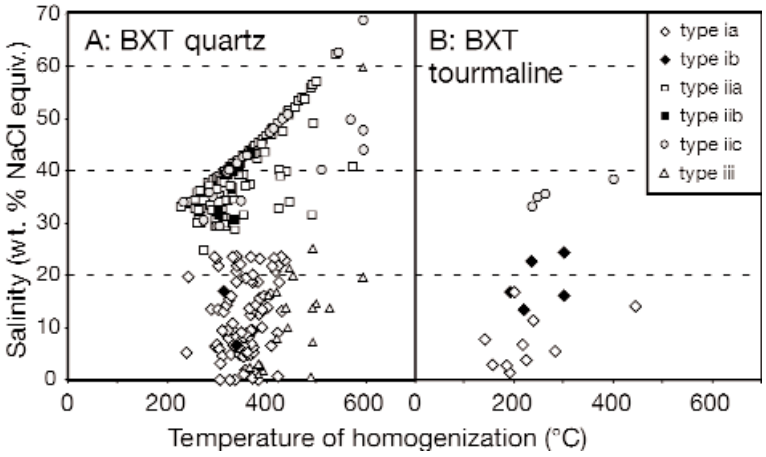

FIG. 15. Temperatures of homogenization vs. salinity (expressed as wt % NaCl equiv) for different fluid inclusion types analyzed from (A) quartz and (B) tourmaline breccia cements. BXT quartz = quartz cement (tourmaline breccia), BXT tourmaline = tourmaline cement (tourmaline breccia). In (A), hypersaline fluid inclusions that homogenize via halite dissolution plot on the "halite trend" of Cloke and Kesler (1979), implying that the fluids may have been halite-saturated prior to their entrapment.

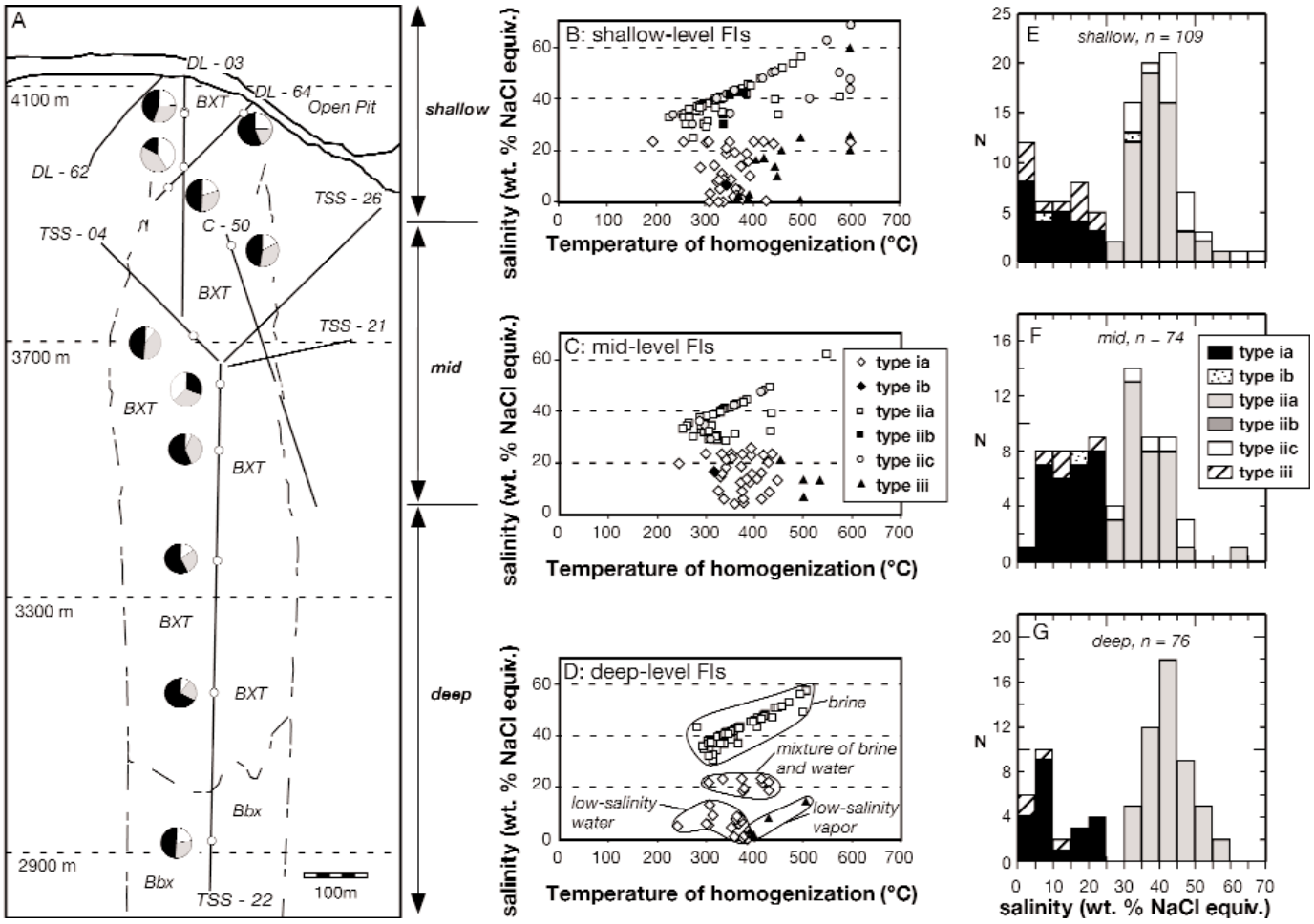

FIG. 16. Spatial variations in homogenization temperatures and salinities of fluid inclusions hosted by quartz cement from the Sur-Sur tourmaline breccia (section XC50, supplemented by data from XC40-XC 70). A. Geologic cross section XC50 (Sur-Sur) showing diamond drill holes and fluid inclusion sample locations (white circles). Pie charts next to each sample location denote the relative proportions of type i (white fill pattern), type ii (gray), and type iii fluid inclusions (black) observed petrographically in individual samples. Also shown are arbitrary spatial subdivisions within the breccia: deep, mid, and shallow levels. Bbx = biotite-cemented breccia, BXT = tourmaline-cemented breccia. B-D. Temperatures of homogenization vs. salinity (expressed as wt % NaCl equiv) for different types of quartz-hosted fluid inclusions from (B) shallow-, (C) middle-, and (D) deep-level samples from the Sur-Sur tourmaline breccia. Note that different fluid types can be discriminated into discrete fields in (D), whereas broad spectrums of data were obtained at middle to shallow levels. E-G. Frequency histograms of salinities (wt % NaCl equiv) for different types of quartz-hosted fluid inclusions from (F) shallow-, (C) middle-, and (D) deep-level samples from the Sur-Sur tourmaline breccia.

TABLE 3. Summary of Fluid Inclusion Data for Quartz- and Tourmaline-Hosted Fluid Inclusions from

Sample no.	Drill hole no.	Cross section	Drill hole depth (m)	Rock type	Cu grade (wt %)	FI types i:ii:iii (%)	FI type	T_f (ºC)	T_f (ºC) (mean)	T_e (ºC)
Quartz-hosted fluid inclusions										
SS221b	TSS-22	XC 50	28	BXTGDCC	2.15	30:35:35	ia			
							iic			
SS123a	E20-A	0	170	BXTGDCC	0.2	32:36:32	ia			
							iia			
SS62b	TSS-22	XC 50	736	BXTGDCC	1.54	22:30:48	ia		–59.0	
							iia			
							iii			
SS224b	TSS-22	XC 50	500–510	BXTGDCC	0.73	9:24:67'	ia	–72.3 to –33.0	–51.6	46.2 to –10.9
							iia			
							iii	–47.1 to –36.0	–42.2	
SS223b	TSS-22	XC 50	300–310	BXTGDCC	0.96	14:29:57	ia			
							iia			
SS222f	TSS-22	XC 50	130–140	BXTGDCC	2.07	6:38:56	ia			
							iia			
SS228f	TSS-4	XC 50	50–60	BXTGDCC	0.96	10:42:48	ia	–82.8 to –38.5	–61.3	–49.2 to –26.0
							iia			
							iii		–70.4	
SS101a	C-50	XC 50	26	BXTGDCC	1.36	17:36:47	ia, ib	–76.3 to –42.0	–57.6	–49.9 to –24.0
							iia		–70.0	
							iii	–71.0 to –43.1	–57.1	–41.5 to –32.3
SSLGS50	DL-64	XC 50	192–200	BXTGDCC	0.6	20:31:49	ia			
							iia, iib			
							iii			
SS230b	DL-64	XC 50	20–30	BXTGDCC	3.91	24:20:56	ia	–72.0 to –41.0	–53.7	
							iia			
							iii			
SS190	DL-03	XC 50	139	BXTGDCC	2.52	41:42:17	ia	–88.6 to –42.5	–56.2	–53.5 to –27.4
							iia			
							iii		–34.9	
SSVHG50a	DL-03	XC 50	56	BXTGDCC	13.85	24:32:44	ia	–74.1 to –49.3	–60.7	
							iia			
							iii			
SSVHG50d	DL-03	XC 50	58	BXTGDCC	9.93		ia, ib	–86.3 to –52.2	–74.3	–58.6 to –32.1
							iia, iic			
							iii		–71.6	
SS490	DL-57	XC 40	85	BXTGDCC	2.46	37:23:40	ia	–65.6 to –41.7	–51.7	–50.4 to –24.7
							iia, iic			
							iii	–75.4 to –53.8	–66.4	
SS524	DL-71	XC 70	99.5	BXTGDCC	2.75	51:05:44	ia	–43.5 to –36.7	–38.7	–30.4 to 2.8
							iia, iic			
							iii		–66.7	
Tourmaline-hosted fluid inclusions										
SS62b	TSS-22	XC 50	736	BXTGDCC	1.54		ia, ib			
							iic	–62.2 to –54.0	–58.1	–50.8 to –41.3
SS223a	TSS-22	XC 50	300–310	BXTGDCC	0.96		ia	–49.2 to –46.0	–48.0	
SS7	TSS-4	XC 50	155	BXTGDCC	1.11		ia, ib	–64.0 to –45.9	–52.5	
SSVHG50d	DL-03	XC 50	58	BXTGDCC	9.93		ia, ib	–59.7 to –49.3	–53.3	–62.4 to –30.6
SS225c	TSS-22	XC 50	609	BXTGDCC	no data		ia	–53.8 to –48.3	–49.7	
Summary data										
Quartz							i	–89.0 to –33.0		–59.0 to 3.0
Quartz							ii			
Quartz							iii	–75.0 to –35.0		–49.0 to –24.0
Tourmaline							i	–64.0 to –46.0		–62.0 to –31.0
Tourmaline							ii			

Notes: Homogenization temperature ranges and means (ºC) for vapor (T_hV), liquid (T_hL), and salts (T_hD), plus salinities (wt % NaCl equiv), freezing

Abbreviations: BXTGDCC = tourmaline breccia (Cascada granodiorite clasts), FI = fluid inclusion, T_hV = vapor homogenization temperature, T_hL = T_f = freezing temperature, T_e = eutectic temperature, T_m = final ice melting temperature

the Sur-Sur Tourmaline Breccia Cement (see text and Fig. 12 for definitions of fluid inclusion types)

T_e (ºC) (mean)	T_m (ºC)	T_m (ºC) (mean)	T_hL (ºC)	T_hL (ºC) (mean)	T_hV (ºC)	T_hV (ºC) (mean)	T_hD_{halite} (ºC)	T_hD_{halite} (ºC) (mean)	Salinity (mean)
	–20.5 to 11.9	–9.0			244.6 to 390.4	323.8			18.4
	–25.4 to 15.0	–5.2			233.5 to 309.3	276.2	137.1 to 416.3	307.6	39.5
	–25.0 to –2.8	–9.4			302.9 to 433.5	351.5			11.9
					242.2 to 495.1	342.5	193.5 to 477.3	332.1	41.6
–26.0	–18.9 to 0.0	–7.2			242.1 to 427.2	360.5			9
					250.6 to 452.6	317.8	214.6 to 505.7	358.0	42.9
		–1.7				390.5			2.9
–30.7	–23.5 to –0.7	–8.9			299.8 to 428.6	357.4			11.4
					242.8 to 498.0	328.0	249.6 to 453.4	364.4	43.3
–23.6	–10.3 to –0.8	–5.3	397.5 to 505.6	451.6		427.3			7.8
	–18.8 to –0.5	–8.3			305.2 to 411.8	355.0			10.8
		–36.3			232.6 to 328.2	280.1	179.1 to 448.2	331.4	40.8
	–20.6 to –3.9	–10.7			331.1 to 444.6	379.9			13.9
					231.1 to 431.6	295.4	130.8 to 383.5	263.9	36.2
–33.5	–23.6 to –2.7	–12.1			309.5 to 446.0	370.1			15
					134.8 to 321.7	259.3	159.4 to 547.0	308.9	39.8
		–17.6		452.4				144.9	20.9
–38.6	–21.1 to –3.1	–12.4			299.4 to 433.7	377.9			15.2
–52.3		18.3			240.0 to 432.0	300.0	137.5 to 338.1	245.3	34.8
–36.9	–9.4 to –4.3	–7.7	499.7 to 534.0	511.2					11.2
	–15.5 to 0.0	–7.6			328.0 to 402.3	356.1			10
					253.1 to 380.1	305.9	103.0 to 462.4	280.3	40.4
		–0.2	408.7 to 497.5	453.1					0.4
	–11.6 to –5.4	–8.5			195.2 to 421.2	348.3			12
		–23.7			241.5 to 322.0	270.2	167.1 to 372.9	285.8	35.8
	–11.7					406.8			15.7
–37.8	–17.3 to –0.3	–7.0			290.8 to 425.4	359.0			9.5
					231.5 to 453.2	285.1	166.1 to 498.8	310.6	39.4
	1.2 to 1.3	1.3	370.2 to 393.1	381.6					2.1
–44.2	–15.1 to 0.1	–7.9			309.5 to 394.0	325.3			10.8
					219.7 to 269.8	245.5	209.2 to 361.0	290.0	37.5
–48.6				>550					
–49.0		–4.2		>600	303.9 to 344.2	324.1		115.0	6.7
					163.4 to >600.0	322.7	156.4 to 552.2	326.5	41.5
		–15.8		>600					19.46
–36.2	–20.6 to –1.1	–9.3			304.3 to 360.5	333.0			11.4
					202.4 to 578.9	306.0	244.2 to 446.7	33.8	41.2
	–23.0 to –0.4	–12.0	352.5 to 425.0	393.7					13.6
–19.1	–5.8 to 20.0	1.9			311.1 to 440.9	362.0			8
					260.8 to 577.3	370.7	238.9 to >600.0	373.7	45.1
–46.3	–16.1 to –6.3	–10.6	396.9 to >600.0	469.4				526.7	25.5
		–22.7			301.6 to 389.7	345.7			23.5
–46.1	–31.7 to –26.7	–29.2			148.1 to 402.6	263.8	217.6 to 303.9	258.8	35.3
	–7.7 to 4.9	–2.0			240.3 to 284.0	262.2			8.2
	–19.9 to –1.5	–9.7			188.9 to 235.4	210.7			12.2
–42.2	–12.0 to 12.9	–3.4			140.5 to 301.9	213.6			13.5
	–10.1 to 0.7	–2.8			156.2 to 445.2	227.0			4.7
	–25.0 to 20.0				195.0 to 446.0				0.0 to 23.0
					135.0 to >600.0		131.0 to >600.0		25.0 to 69.0
	–23.0 to 1.0		353.0 to >600.0						0.0 to 59.0
	–23.0 to 13.0				141.0 to 445.0				1.0 to 23.0
					148.0 to 403.0		217.0 to 304.0		33.0 to 38.0

temperatures (T_f), temperatures of first ice melting (T_e,) and temperatures of final ice melting T_m
liquid homogenization temperature, T_hD_{halite} = halite dissolution temperature, $T_hD_{sylvite}$ = sylvite dissolution temperature,

3, Fig.14A). Halite dissolution temperatures (T_hD_{halite}) for type ii fluid inclusions are between 131° and >600°C, however sylvite dissolution temperatures ($T_hD_{sylvite}$) for type ii fluid inclusions are 180° to 194°C (Table 3). Measured freezing temperatures (T_f) for type i fluid inclusions vary widely, between –89° and –33°C (Table 3, Fig. 14E). Freezing temperatures for type iii fluid inclusions also vary markedly (–75° to –35°C). Eutectic temperatures (T_e) for type i fluid inclusions range from –59° to 3°C, however type iii fluid inclusions have a narrower range of eutectic temperatures between –49° and –24°C (Table 3; Fig. 14G). Final ice melting temperatures (T_m) for type i fluid inclusions are between –25° to –20°C (Table 3; Fig. 14E), and for type iii fluid inclusions are from –23° to 1°C (Fig. 14I).

Based on the measured freezing point depressions and salt dissolution temperatures, a range of salinities has been calculated for the quartz-hosted fluid inclusions from Sur-Sur (Figs. 14C, 15A). The brines, gases, and low-salinity aqueous liquids define a continuum from dilute (~0 wt % NaCl equiv) to hypersaline (69 wt % NaCl equiv) compositions. Most of the salinities calculated for type ii salt-saturated fluid inclusions are between 30 and 50 wt percent NaCl equiv (Fig. 14C).

Tourmaline-hosted fluid inclusions

Microthermometric analyses were performed on 23 fluid inclusions in tourmaline from five samples of tourmaline breccia. These included type ia (n = 14), type ib (n = 5), and type iic (n = 4; Fig. 14B, D, F, H, J) fluid inclusions. Samples were collected from section XC 50ss between 2,919- and 4,064-m elevation. Type i inclusions are the most abundant, but rare type ii inclusions are also present. The fluid inclusions are generally small (5–40 μm) and elongate due to their growth along cleavage planes. Daughter minerals in tourmaline-hosted type ii fluid inclusions include halite, hematite, and opaques.

Vapor homogenization temperatures for tourmaline-hosted type i and ii fluid inclusions range from 141° to 445°C (Table 3; Fig. 14B). Halite dissolution temperatures for type ii fluid inclusions are between 217° and 304°C. Freezing temperatures for type i fluid inclusions are from –64° to –46°C (Fig. 14F). Eutectic temperatures for type i fluid inclusions are from –62° to –31°C (Fig. 14H), and final ice melting temperatures for type i fluid inclusions are from –23° to 13°C (Fig. 14J). Salinities calculated for type i fluid inclusions range from 1 to 23 wt percent NaCl equiv with most values between 1 and 15 wt percent NaCl equiv. Type ii fluid inclusions have a narrow range of calculated salinities between 33 and 38 wt percent NaCl equiv (Table 3; Figs. 14D, 15B).

Fluid types and spatial variations

Coexisting type i and iii fluid inclusions within individual secondary trails (Fig. 13C) define a distinctive fluid inclusion assemblage within quartz cement in the tourmaline breccia. These inclusions have similar T_hV and T_hL (mostly between 350° and 400°C) and are interpreted to indicate the presence of two fluids (low-salinity water and gas) at the time of entrapment. A second distinctive fluid inclusion assemblage is defined by trails that contain coexisting type ii and iii fluid inclusions. This assemblage has been observed in samples from the highest elevations of the breccia complex (samples SSVHG50d and SS524 at 4,064- and 4,032-m elev, respectively; Fig. 13D, E). These inclusions had consistently high homogenization temperatures (>500°C) for both halite and vapor (Table 3) and indicate that high-temperature hypersaline brine and gas coexisted in the highest parts of the breccia complex at the time of entrapment. Furthermore, the type ii fluid inclusions that homogenized by salt dissolution plot in the halite trend of Cloke and Kesler (1979), indicating that the fluids may have been saturated with halite before entrapment (Figs. 15A, 16B-D).

Although observations of coexisting fluid phases are limited to a few secondary trails in quartz cement, the range of salinity determined for the Sur-Sur tourmaline breccia suggests the possibility of the coexistence of multiple fluid phases during cementation. The greatest range in homogenization temperatures has been obtained at the shallowest levels (Fig. 16B), with the range of T_h values becoming somewhat narrower at depth (Fig. 16D). Halite-saturated inclusions (type iia) are present throughout the vertical extent of the breccia. Multiphase fluid inclusions (type iic) occur only at mid- to shallow-level depths (Fig. 16B, C). Type iii vapor-rich fluid inclusions commonly have higher homogenization temperatures than type i liquid-rich inclusions but overlap where type i and iii fluid inclusions occur in the same samples (Fig. 16). The highest temperatures of homogenization of type iii fluid inclusions also were found at shallow levels.

The salinities of the inclusions also seem to indicate the presence of both low-salinity aqueous liquid and high-salinity brine at depth (Fig. 16D). A third grouping of type i fluid inclusions with salinities around 20 wt percent NaCl equiv may be the product of mixing between these two end members. At mid and shallow levels, the distinctions are less obvious, also suggesting possible fluid mixing (Fig. 16B, C).

Lead Isotopes

Extensive lead isotope data are available for central Chile (Tilton, 1979; Hildreth and Moorbath, 1988; Puig, 1988; Zentilli et al., 1988; Davidson et al., 1991; Kay and Ambruzzi, 1996; Tosdal and Munizaga, 1996, 2003; Kay et al., 1999; Fig. 17). These data cover the Central volcanic zone (CVZ) and the Southern volcanic zone (SVZ) between 22º and 38º30'S, including the flat slab zone from 28º to 33ºS (Fig. 17). Lead isotope analyses of sulfides from the Río Blanco-Los Bronces ore deposit (Tilton, 1979; Puig, 1988; Zentilli et al., 1988; Tosdal and Munizaga, 1996, 2003) comprise a well-homogenized, closely spaced cluster within the field for the regional volcanic rocks of the Southern volcanic zone (Fig. 17).

In this study, the isotopic composition of lead was determined in two samples of anhydrite cement from the Río Blanco magmatic breccia and two samples from the Sur-Sur tourmaline breccia (Table 4). Textural relationships indicate that the anhydrite precipitated prior to sulfide deposition. No analyses of the Pb content of the samples were obtained but a subsequent study of lead in anhydrite from the oxide stage of the El Teniente deposit of central Chile (Cannell, 2004) determined Pb contents of 0.5 to 25 ppm and similar isotopic ratios.

The isotopic compositions of lead in anhydrite from Río Blanco-Los Bronces are distinctly less radiogenic than that of

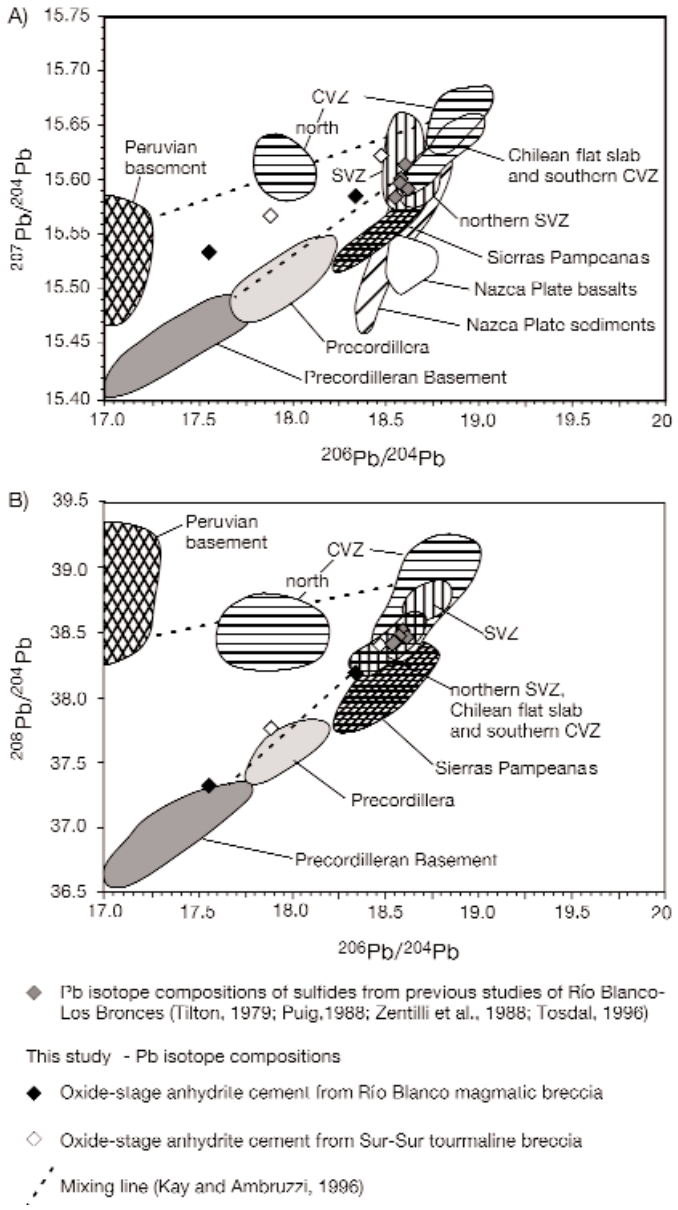

FIG. 17. Uranogenic and thorogenic diagrams showing lead isotope compositions for regional volcanic rocks in central Chile, sulfides from the Río Blanco-Los Bronces ore deposit, and anhydrite cement from the Río Blanco-Los Bronces ore deposit (this study). Data for regional rocks are from Kay et al. (1999). Sulfide data from Tilton (1979), Puig (1988), Zentilli et al. (1988), and Tosdal and Munizaga (1996). The sulfide minerals and igneous wall rocks at Rio Blanco-Los Bronces have more radiogenic lead isotope compositions than anhydrite, which appears to plot on mixing lines between the sulfide ores and Precordilleran (B) or Peruvian basement (A).

the ores and local host rocks. They define an array of values in Figure 17 from the least radiogenic lead, found in anhydrite cement from the Río Blanco magmatic breccia, to the most radiogenic lead, found in anhydrite cement in the Sur-Sur tourmaline breccia. The most radiogenic lead in anhydrite is similar in isotopic composition to the lead in the sulfides. Lead isotope data are not available on more refractory minerals of the oxide stage from Río Blanco. It is unlikely that the lead isotope compositions of anhydrite from Río Blanco have been reset by later fluids, as there is no petrographic evidence of alteration of the anhydrite samples. Our samples were collected at elevations between 2,846 and 3,541 m (Table 4), beneath the domain of supergene anhydrite dissolution documented by Vargas et al. (1999).

TABLE 4. Lead Isotope Compositions of Anhydrite Cement from the Sur-Sur Ttourmaline Breccia and Río Blanco Magmatic Breccia

Sample no.	DDH	Altitude (m)	$^{206}Pb/^{204}Pb$	$^{207}Pb/^{204}Pb$	$^{208}Pb/^{204}Pb$
RB246h	DDH-450	2,846	17.558	15.534	37.341
RB240b	DDH-450	3,078	18.345	15.586	38.205
SS01BXT12	TSS-12	3,541	17.892	15.567	37.774
SS60c	TSS-22	3,077	18.479	15.623	38.412

Abbreviations: DDH = diamond drill hole

The lead isotope data appear to indicate that the fluids that precipitated anhydrite at Río Blanco-Los Bronces were distinct from the sulfide-forming fluids, at least in terms of their lead isotope compositions. The sulfides at Río Blanco-Los Bronces have a magmatic-hydrothermal source of lead that is identical to the igneous intrusions and volcanic rocks that host the deposit (Tosdal and Munizaga, 2003). The earlier formed anhydrite must have incorporated lead from sources distinct from the local intrusions and volcanic wall rocks. One of those sources was probably the Precordilleran basement, as the thorogenic ($^{208}Pb/^{204}Pb$) isotope compositions for anhydrite cement form a linear trend that extends from the Chilean flat slab field toward the least radiogenic field for the Precordilleran basement and Precordillera (Fig. 17). However, the equivalent trend of $^{207}Pb/^{204}Pb$ data lies between Precordilleran rocks in central Chile and the basement rocks from Peru, implying a more complex origin for the lead deposited with the anhydrite.

Discussion

Constraints on temperature and redox conditions

The main stage of chalcopyrite deposition in the sulfide cement at Sur-Sur is estimated to have occurred at temperatures of approximately 450° to 300°C, based on the range of temperatures of homogenization obtained from fluid inclusions in quartz cement (Fig. 14A). From Figure 18A, the oxygen fugacity (f_{O_2}) of hydrothermal fluids is interpreted to have varied by 4 to 5 log units, from specularite stable through tourmaline ± magnetite stable, to biotite ± magnetite stable conditions. The lower limit of $\log f_{O_2}$ values in Figure 18A is defined by the reaction of schorl (Fe tourmaline) to annite (Fe biotite):

$$NaFe_3Al_6(Si_6O_{18})(BO_3)_3(OH)_{4\,(s)} + 6KCl_{(aq)} + 12SiO_{2\,(s)} + 5Fe_3O_{4\,(s)} + 11H_2O_{\,(l)}$$
$$= 6KFe_3AlSi_3O_{10}(OH)_{2\,(s)} + 5HCl_{(aq)} + NaCl_{(aq)} + 3H_3BO_{3(aq)} + 2.5O_{2(g)}.$$

The position of the tourmaline and/or biotite transition in Figure 18A is dependent on the composition of biotite and tourmaline, the activity of H_3BO_3 and the ratios a_{NaCl}/a_{HCl} and a_{KCl}/a_{HCl}, the latter constrained by a section on an a_{NaCl}/a_{HCl}

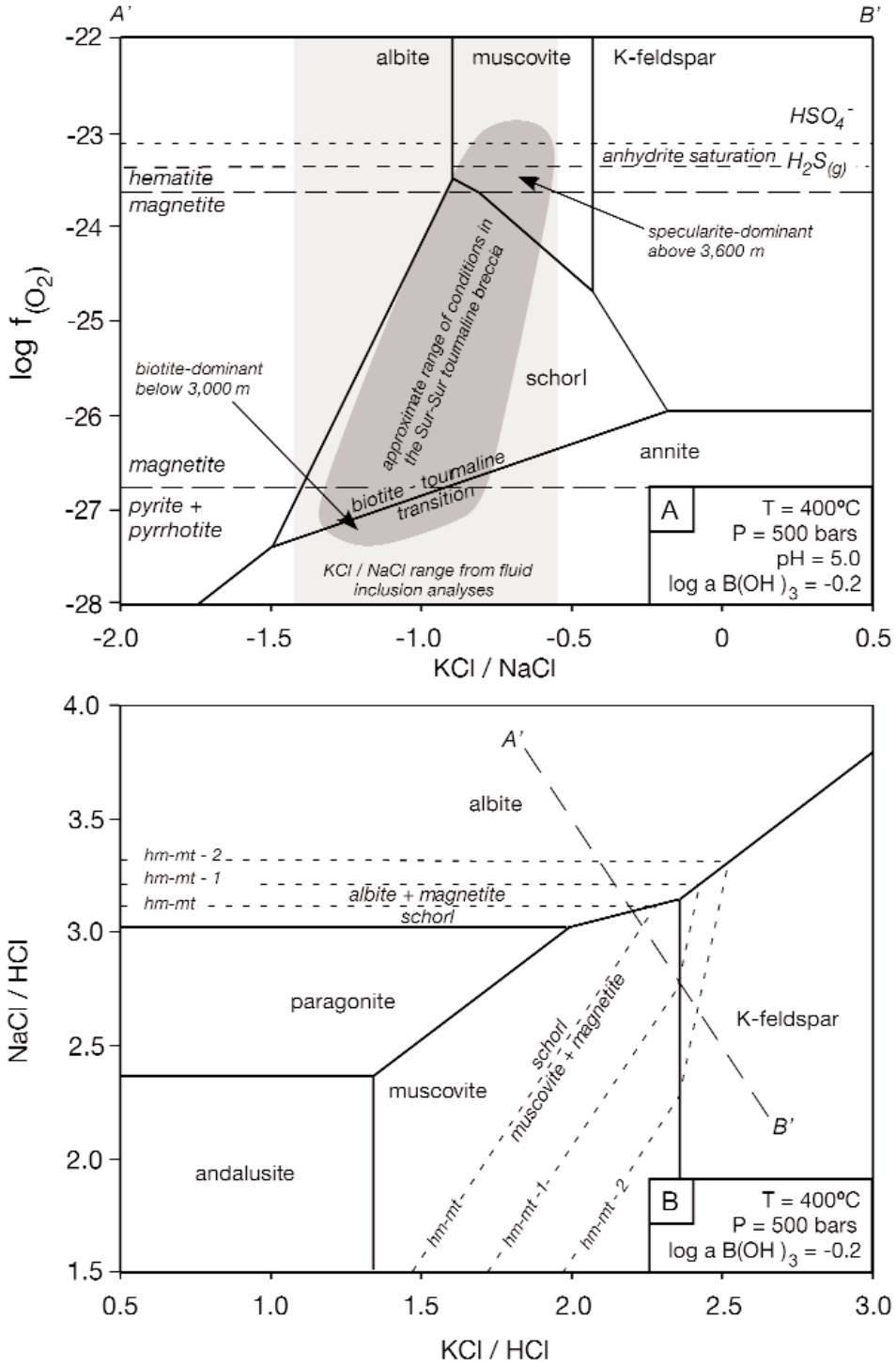

FIG. 18. A. Log $f_{O_2(g)}$ vs. log aKCl$_{(aq)}$/NaCl$_{(aq)}$ diagram at 400°C and 500 bars, showing the stability of schorl (Fe tourmaline) with respect to albite, muscovite, K-feldspar, and annite (Fe biotite). The inferred range of redox conditions in the Sur-Sur tourmaline breccia (dark-gray shaded field) is defined from the mineralogy and the K/Na ratio of fluid inclusions (light-gray shaded box; Frikken, 2004). The diagram is constructed assuming log activity of $B(OH)_3$ = –0.2, log aKCl$_{(aq)}$/HCl$_{(aq)}$ and log aNaCl$_{(aq)}$/HCl$_{(aq)}$ values constrained by section A'-B' in (B) and quartz, magnetite ± hematite in excess. The anhydrite saturation surface has been drawn assuming pH = 5, log activity $H_2S_{(aq)}$ = –2 and log aCaCl$_{2(aq)}$/(HCl$_{(aq)}$)^2 = 3. B. Log aKCl$_{(aq)}$/HCl$_{(aq)}$ vs. log aNaCl$_{(aq)}$/HCl$_{(aq)}$ diagram at 400°C and 500 bars, illustrating the conditions (A'-B') used in construction of (A). The section was drawn such that tourmaline may coexist with albite, muscovite, and K-feldspar in the presence of excess quartz and magnetite ± hematite (e.g., hm-mt-1 refers to log f_{O_2} one unit below hematite-magnetite equilibrium). Contours illustrate the schorl boundary at different oxidation states, given relative to the hematite and/or magnetite buffer. Thermodynamic data for schorl from Garofalo et al. (2000); other data from FreeGs: web-enabled thermodynamic database for modeling of geochemical processes (Bastrakov et al., 2004 <www.agso.gov.au/rural/projects/geofluids.jsp>).

versus a_{KCl}/a_{HCl} diagram (Fig. 18B). The biotite cement from Sur-Sur has magnesium numbers (Mg # = 100*Mg/Mg + Fe) of 55 to 65, based on electron microprobe analyses (Frikken, 2004), indicating compositions intermediate between phlogopite and annite end members. Electron microprobe analyses of tourmaline cement (Frikken, 2004) indicate compositions that are intermediate between dravite (Mg tourmaline) and schorl, with a component of elbaite, the Li-Al–rich end member. The Mg # of tourmaline is more variable than that of biotite, ranging between 20 and 80 with most values between 40 and 60 (Frikken, 2004). Based on our calculations, the stability of schorl with respect to annite, albite, muscovite, and K-feldspar is also relatively insensitive to temperature from 350° to 450°C. Based on the observed mineralogy (Fig. 2), the oxygen fugacity of hydrothermal fluids at Sur-Sur decreased from specularite stable at high altitudes (Fig. 6D) through biotite and magnetite stable at depth, notably below 3,000 m at Sur-Sur and also below about 3,300 m in the Don Luis sector (Fig. 6A).

Sulfur isotope zonation

The observed mineralogical zonation at Sur-Sur is coincident with the zonation of sulfur isotope compositions of sulfides from near-zero values at depth to values of –4 per mil at the top of the breccia. The distinctly negative sulfur isotope values obtained for chalcopyrite at high altitude (>3,700 m asl) in the Sur-Sur tourmaline breccia correlate with zones of high copper grade (Fig. 10), abundant specularite (or anhydrite at depth), and vuggy textures. This transition occurs over a vertical interval of approximately 100 m (Fig. 10).

The extent of redox-controlled isotopic fractionation of sulfur isotopes depends on the initial ratio of aqueous sulfate to aqueous sulfide (R value) and also on any influences imposed by external sulfur reservoirs (Ohmoto and Goldhaber, 1997). For example, if we assume a bulk sulfur composition of +1 per mil, ranges of chalcopyrite and anhydrite compositions similar to those measured from Sur-Sur are predicted to precipitate from a reduced fluid (R = 0.25) that undergoes cooling from approximately 450° to 300°C (Fig. 19A). This range of temperatures is consistent with the bulk of the fluid inclusion data from Sur-Sur (Fig. 14). Although this is a nonunique result, Figure 19A shows that the observed range of $\delta^{34}S$ values of sulfide and sulfate minerals at Sur-Sur (e.g., –4.1 to +13.4‰) can be produced by precipitation from a cooling, reduced fluid. However, the large decrease in $\delta^{34}S$ values to –5 per mil over a vertical interval of ~100 m (Fig. 10) would require approximately 150°C of cooling (Fig. 19A) over a very narrow vertical interval. Such enormous temperature gradients are rare in hydrothermal systems, except as a result of fluid mixing, which would be consistent with the measured range of salinity data from fluid inclusions (Fig. 15).

Alternatively, exsolution of magmatic SO_2 could have produced a shallow crustal fluid reservoir enriched in SO_2 or SO either through condensation into meteoric water or through disproportionation of the magmatic gas; Rye, 1993). In this case, the oxidized fluid is assumed to have a bulk sulfur isotope composition of +11.2 per mil (the lowest $\delta^{34}S$ sulfate value measured from the Sur-Sur tourmaline breccia cement; Table 2). Assuming that the fluid in this scenario is highly oxidizing (R = 0.9), the range of sulfide sulfur isotope compositions predicted to form at temperatures of 450° to 300°C would be comparable to those observed at shallow levels in the Sur-Sur tourmaline breccia (Fig. 19B). In this case, extreme temperature gradients are again required. Such gradients may have occurred if the SO_2-bearing magmatic gas condensed into lower temperature meteoric ground water or some external water at the top of the breccia body.

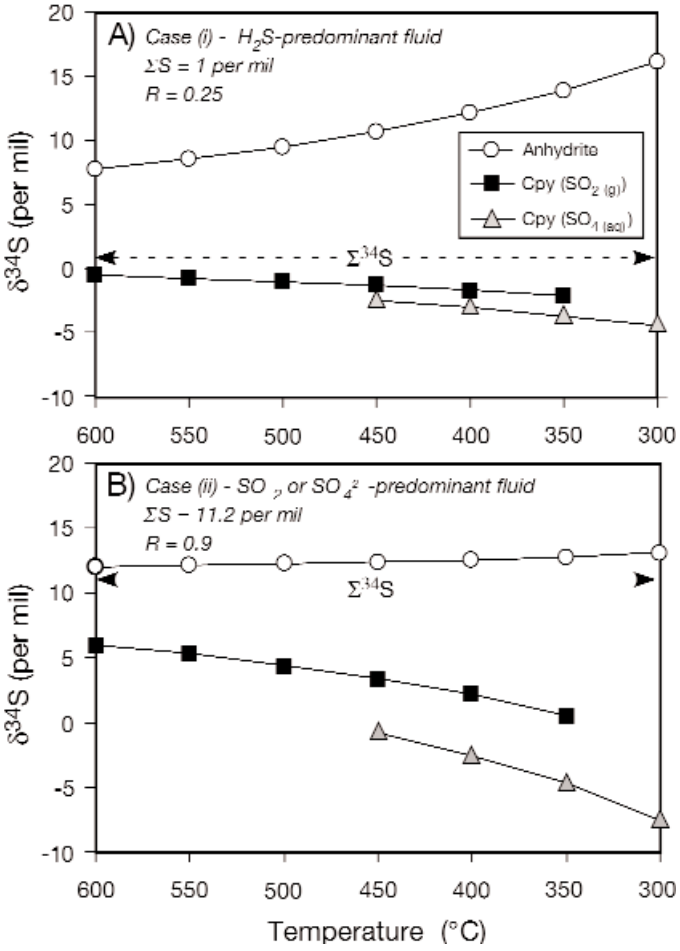

FIG. 19. A. Calculated sulfur isotope compositions for sulfate-sulfide equilibria as a function of temperature (°C) vs. $\delta^{34}S$ (‰), assuming a total sulfur content of 1 per mil and $m\Sigma_{SO_4}/m\Sigma_{H_2S}$ value (R value) of 0.25 (i.e., reduced, H_2S-predominant fluid). Two curves for chalcopyrite compositions are shown: chalcopyrite compositions precipitated from an SO_2-bearing fluid and chalcopyrite precipitated from an SO_4^{2-} -bearing fluid (Ohmoto and Goldhaber, 1997). $SO_{2(g)}$ undergoes disproportionation to aqueous sulfate at approximately 400°C, but kinetics may inhibit the onset of this transition in natural systems. Hence, some overlap of temperatures has been plotted for the two curves. B. Calculated sulfur isotope compositions for sulfate-sulfide equilibria as a function temperature (°C) vs. $\delta^{34}S$ assuming a total sulfur content of 11.15 per mil and an $m\Sigma_{SO_4}/m\Sigma_{H_2S}$ value of 0.9 (i.e., oxidized, SO_2-predominant fluid). As for (A), two curves for chalcopyrite compositions are shown: chalcopyrite compositions precipitated from an SO_2-bearing fluid and chalcopyrite precipitated from an SO_4-bearing fluid (Ohmoto and Goldhaber, 1997).

Fluid sources

Oxygen-deuterium analyses of cements and alteration minerals from Río Blanco-Los Bronces have indicated that the hydrothermal fluids were predominantly magmatic

(Kusakabe et al., 1984, 1990; Skewes et al., 2003). At Sur-Sur, the presence of hypersaline brine inclusions in the breccia cement is also strong evidence for a magmatic fluid, consistent with a magmatic-hydrothermal origin for the Sur-Sur tourmaline breccia.

The lead isotope compositions of sulfides from the cement in the mineralized breccia indicate a well-homogenized source. They have a lead isotope signature similar to igneous rocks of the Southern volcanic zone. In contrast, anhydrite cements from Sur-Sur and Río Blanco have lead isotope compositions that are distinct from the host rocks and sulfide minerals (Fig. 17). This less radiogenic lead is isotopically comparable to the Precordilleran basement and Precordillera of central Chile (Fig. 17). The presence of exotic lead in anhydrite implies that the oxide-stage fluid at Sur-Sur must have been sourced at least in part from outside the magmatic-hydrothermal system and surrounding wall rocks. The fluid could have been meteoric ground water, connate water from the underlying evaporite-bearing Jurassic sedimentary rocks (Fig. 1A), metamorphic water from the lower crust (e.g., Kay et al., 1999) or a fluid from some other source. High-temperature exchange of ^{18}O between the external fluid and the local igneous wall rocks may explain why O-D studies have failed to clearly identify external fluids at Río Blanco-Los Bronces (e.g., Kusakabe et al., 1984, 1990; Skewes et al., 2003).

Genetic model

In shallow crustal settings, exsolution of hydrothermal fluids from a crystallizing magma can result in the generation of large volumes of gases, including oxidizing components such as $SO_{2(g)}$, acidic components such as $HCl_{(g)}$, and smaller volumes of dense, saline brine (Henley and McNabb, 1978; Burnham, 1979; Bodnar et al., 1985). The formation of magmatic-hydrothermal breccia requires catastrophic brittle failure of the crystallizing intrusion, and the overlying rock column when hydrostatic pressures exceed both lithostatic load and the tensile strength of the host rocks (Burnham, 1979, 1985). Under these conditions, aqueous phase separation will have occurred from the melt during brittle failure, releasing magmatic gas and hypersaline brine (e.g., Bodnar et al., 1989; Fournier, 1999).

In Figure 20A, we speculate that during the oxide stage, initial brecciation was triggered by magmatic fluid exsolution. Creation of a fractured rock column above the magma allowed SO_2-rich, buoyant gas to separate physically from the coexisting brine. The gas ascended through and was trapped at the top of the blind breccia column (either by the termination of the fracture array or by water descending into the breccia from the overlying rock column), producing a shallow crustal fluid reservoir enriched in SO_2 or SO_4^{2-} (either through condensation into meteoric water or through magmatic gas disproportionation; Rye, 1993). This fluid could have absorbed all or part of the magmatic gas plume, generating a hybrid oxidized, acidic fluid that contained SO_2, HCl, and possibly B, and which had the capacity to cause intense quartz-sericite-tourmaline alteration. This hybrid fluid would have contained magmatic sulfur (derived from $SO_{2(g)}$) and also appears to have contained exotic lead, based on the lead isotope composition of anhydrite. The density contrasts between the brine and vapor were such that the dense brine remained near the magmatic source at this time.

Brine migration upward through the breccia at the time of copper sulfide deposition (mineralization stage) is assumed to correspond to a period of magma resurgence (Fig. 20B). The upsurge in brine or brine plus additional vapor would have been driven by pressure differentials within the magmatic-hydrothermal system; either tectonic or magmatic. Mixing of copper-rich brine and the high-level reservoir of acidic, oxidized water (Fig. 20B) is inferred to have caused

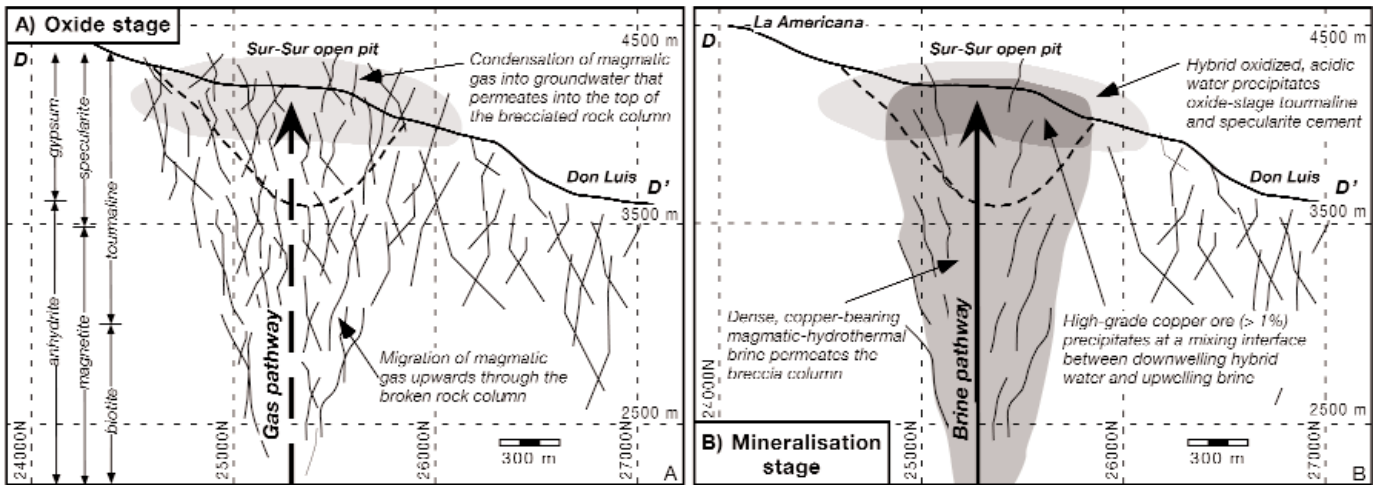

FIG. 20. Schematic diagram showing possible fluid evolution in the Sur-Sur tourmaline breccia. A. Magmatic-hydrothermal brecciation triggered by a deep-seated crystallizing intrusion allowed magmatic gases and hypersaline brines to exsolve from the melt. Expansion of low-density steam propagated the brecciation front upward and outward from the initial explosion point. Ground waters permeated into the upper and outer parts of the brecciated rock column, condensing magmatic gases and producing an acidic, oxidized hybrid water that precipitated oxide-stage specularite, tourmaline, and anhydrite and caused widespread quartz-sericite-tourmaline alteration. B. Upwelling of the dense, copper-bearing magmatic-hydrothermal brine caused deposition of chalcopyrite through the breccia column. The highest ore grades developed at the top of the breccia column due to mixing of the brine with the oxidized hybrid water.

the transition from chalcopyrite-magnetite to chalcopyrite-specularite and finally pyrite-specularite mineralization, as well as the high-grade copper mineralization at the top of the breccia column. Precipitation of chalcopyrite would have been promoted by changes in temperature, pressure, the oxidation state of the fluids, well as changes in acidity, salinity, and activity of the sulfur species. The gradients in redox potential and activity of sulfur caused by mixing of hypersaline brine and low-salinity fluid were the most important factors controlling chalcopyrite precipitation in the Sur-Sur tourmaline breccia, although high-temperature phase separation of magmatic-hydrothermal gases and brines also may have caused precipitation of at least some of the sulfides.

Given that most of the ore occurs in pore spaces within the breccias, water-rock interaction was probably not a major ore-forming process. In Figure 21 the precipitation mechanism is modeled as oxidation of relatively reduced brine, which would account for the highest grades of chalcopyrite occurring with specularite in the upper parts of the Sur-Sur tourmaline breccia.

Concluding Remarks

The Sur-Sur tourmaline breccia is an intensely fractured and altered column of rock that has been cemented by variable amounts of hydrothermal tourmaline, specularite, sulfides, anhydrite, magnetite, and quartz. The presence of high-temperature hypersaline fluid inclusions confirms a magmatic-hydrothermal origin for the breccia that must have been sourced from a crystallizing intrusion emplaced at some unknown depth below the currently explored mine levels. The remarkably simple paragenesis and the lack of any re-brecciated mineralization imply that the Sur-Sur tourmaline breccia was cemented during one major hydrothermal event. This was triggered by a catastrophic magmatic-hydrothermal explosion which formed the >3-km-long and >1,200-m-high breccia dike. The explosion fractured the San Francisco batholith extensively, and irreversibly and instantaneously changed the hydrology and confining pressures of the magmatic-hydrothermal system, creating new space into which brines, low-salinity aqueous fluid and gases could migrate readily.

We have documented mineralogical and isotopic zonations that provide evidence for fluid mixing, phase separation, oxidation, and water-rock interaction during the formation of the Sur-Sur breccia. While all of these processes were important for the formation of the magmatic-hydrothermal breccia, we interpret that high-grade ore formed at the top of the system mainly due to fluid mixing.

Acknowledgments

This work was undertaken as part of the senior author's Ph.D. dissertation, and the Australian Research Council is thanked for the provision of an Australian Postgraduate Award (Industry) for the duration of the project. Many thanks are extended to the geological staff from CODELCO for providing datasets and logistical support for fieldwork at Río Blanco and for numerous constructive discussions. Financial support for this research project by the industry sponsors of

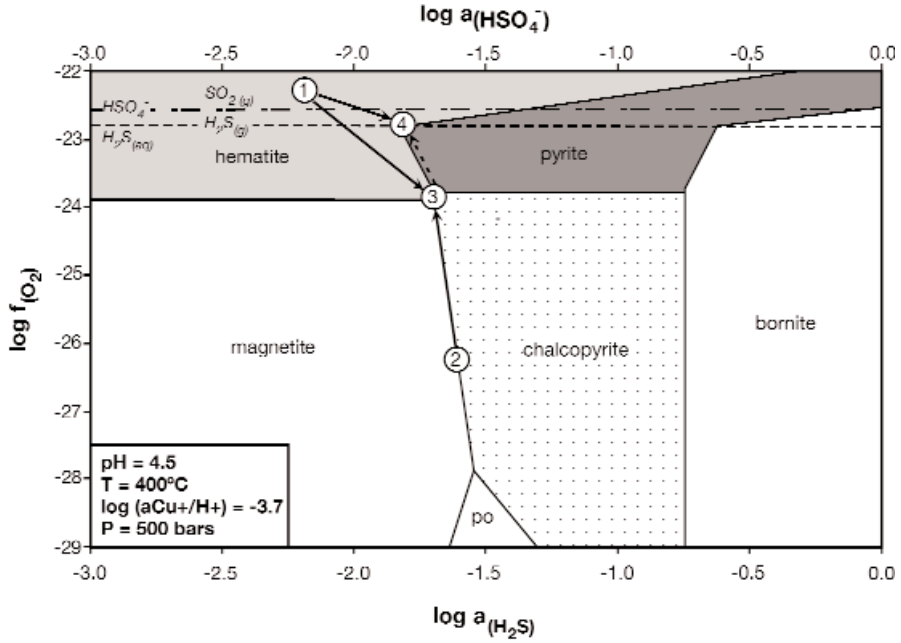

FIG. 21. Phase diagram showing copper Fe sulfide and oxide stability fields as a function of oxygen fugacity and aqueous sulfur activity. Numbered circles schematically illustrate fluid evolution through the Sur-Sur breccia complex. 1 = estimated initial hybrid fluid composition (specularite stable and oxidizing; i.e., HSO_4^- or SO_2 predominant); 2 = estimated mineralizing brine composition (chalcopyrite-magnetite stable and reducing; i.e., H_2S predominant); 3 = mixture of brine and hybrid fluid, dominated by brine (chalcopyrite-specularite stable, reducing; i.e., H_2S predominant); 4 = mixture of brine and hybrid fluid, dominated by water (pyrite-specularite stable, oxidizing; i.e., HSO_4^- predominant) producing the barren cements that occur at the highest elevations in the tourmaline breccia (pyrite, specularite, and tourmaline). This diagram was constructed assuming T = 400°C, P = 500 bars, pH = 4.5, and $\log a_{(Cu+/H+)} = -3.7$. Thermodynamic properties generated from SUPCRT92 (Johnson et al., 1992).

Australian Mineral Industry Research Association (AMIRA) project P511 is gratefully acknowledged. The Central Science Laboratory is thanked for assistance in generating sulfur isotope results, and John Foden (University of Adelaide) is thanked for undertaking the radiogenic isotope analyses. Garry Davidson is thanked for assistance with the sulfur isotope modeling. We also thank Glen Masterman for his assistance in the use of MapInfo software, Simon Stevens for the preparation of polished thin sections, and Andrew Rae for his assistance with the fluid inclusion facility. This manuscript has benefited considerably from reviews by Steve Kesler, Keiko Hattori, Bill Atkinson, Roger Skirrow, and Mark Hannington. Dick Tosdal, Graham Carr, and Cari Deyell are also thanked for useful discussions. We gratefully acknowledge the support of the Australian Research Council through the Special Research Centre program and the Linkage grant scheme.

November 15, 2004; July 15, 2005

REFERENCES

Bastrakov, E., Shvarov, Y., Girvan, S., Cleverley, J., and Wyborn, L., 2004, FreeGs: Web-enabled thermodynamic database for modelling of geochemical processes [abs.]: Geological Society of Australia Abstracts, v. 73, p. 52.

Bodnar, R.J., Burnham, C.W., and Sterner, S.M., 1985, Synthetic inclusions in natural quartz. III. Determination of phase equilibrium properties in the system H_2O-NaCl to 1000ºC and 1500 bars: Geochimica et Cosmochimica Acta, v. 49, p. 1861–1873.

Bodnar, R.J., Sterner, S.M., and Hall, D.L., 1989, Salty: A FORTRAN program to calculate compositions of fluid inclusions in the system NaCl-KCl-H_2O: Computers and Geosciences, v. 15, p. 19–41.

Burnham, C.W., 1979, Magmas and hydrothermal fluids, *in* H. L. Barnes, ed., Geochemistry of hydrothermal ore deposits, 2nd ed.: New York, John Wiley and Sons, p. 71–136.

——1985, Energy release in subvolcanic environments: Implications for breccia formation: Economic Geology, v. 80, p. 1515–1522.

Camus, F., 2002, The Andean porphyry systems: University of Tasmania, Centre for Ore Deposit Research Special Publication 4, p. 5–22.

Cannell, J.B., 2004, El Teniente porphyry copper-molybdenum deposit, central Chile: Unpublished PhD thesis, Australia, University of Tasmania, 341 p.

Cloke, P.L., and Kesler, S.E., 1979, The halite trend in hydrothermal systems: Economic Geology, v. 74, p. 1823–1831.

Davidson, P., and Kamenetsky, V. S., 2001, Immiscibility and continuous melt-fluid evolution within the Río Blanco porphyry system, Chile: Evidence from inclusions in magmatic quartz: Economic Geology, v. 96, p.1921–1929.

Davidson, J.P., Harmon, R.S., and Wörner, G., 1991, The source of central Andean magmas: Some considerations: Geological Society of America Special Paper 265, p. 233–244.

Davidson, P., Kamenetsky, V.S., Cooke, D.R., Frikken, P., Hollings, P., Ryan, C, Van Achterbergh, E., Mernagh, T., Skarmeta, J., Serrano, L., and Vargas, R, 2005, Magmatic precursors of hydrothermal fluids at the Rio Blanco Cu-molybdenum deposit, Chile: Links to silicate magmas and metal transport: Economic Geology, v. 100, p. 963–978.

Deckart, K., Clark, A.H., Aquilar, C., and Vargas, R, 2005, Magmatic and hydrothermal chronology of the supergiant Rio Blanco porphyry copper deposit, central Chile: Implications of an integrated U-Pb and ^{40}Ar-^{39}Ar database: Economic Geology, v. 100, p. 905–934.

Fournier, R.O., 1999, Hydrothermal processes related to movement of fluid from plastic into brittle rock in the magmatic-epithermal environment: Economic Geology, vol. 94, 8, p. 1193–1211.

Frikken, P.H., 2004, Breccia-hosted copper-molybdenum mineralization at Río Blanco, Chile: Unpublished PhD thesis, Australia, University of Tasmania, 290 p.

Garofalo, P., Audétat, A., Günther, D., Heinrich, C.A., and Ridley, J., 2000, Estimation and testing of standard molar thermodynamic properties of tourmaline end-members using data of natural samples: American Mineralogist, v. 85, p. 78–88.

Gustafson, L.B., and Hunt, J.P., 1975, The porphyry copper deposit at El Salvador, Chile: Economic Geology, v. 70, p. 857–912.

Henley, R.W., and McNabb, A., 1978, Magmatic vapor plumes and groundwater interaction in porphyry copper emplacement: Economic Geology, v. 73, p. 1–20.

Hildreth, W., and Moorbath, S., 1988, Crustal contributions to arc magmatism in the Andes of central Chile: Contributions to Mineralogy and Petrology, v. 98, p. 455–498.

Hollings, P., Cooke, D., and Clark, A., 2005, Regional geochemistry of Tertiary igneous rocks in Central Chile: Implications for the geodynamic environment of giant porphyry copper and epithermal gold mineralization: Economic Geology, v. 100, p. 887–904.

Holmgren, C., Marti, M., Skewes, M.A., Schneider, A., and Harmon, R., 1988, Análisis isotópicos y de inclusiones fluidas en el yacimiento Los Bronces, Chile central: Congreso Geológico Chileno, no. 5, Actas, v. 1, p. B299–B314.

Huston, D.L., Power, M., and Large, R.R., 1993, Laser-ablation analysis of sulfur isotopes: An analytical technique now available in Australia [abs]: Geological Society of Australia Abstracts v. 10, p. 30–31.

Johnson, J.W., Oelkers, E.H., and Helgeson, H.C., 1992, SUPCRT92: A software package for calculating the standard molal thermodynamic properties of minerals, gases, aqueous species and reactions from 1 to 5000 bars and 0° to 1000°C: Computers and Geosciences, v. 18, p. 899–947.

Kay, S.M., and Ambruzzi, J.M., 1996, Magmatic evidence for Neogene lithospheric evolution of the central Andean "flat slab" between 30–32 degrees south: Tectonophysics, v. 259, p. 15–28.

Kay, S.M., Mpodozis, C., and Coira, B., 1999, Neogene magmatism, tectonism and mineral deposits of the central Andes: Society of Economic Geologists Special Publication 7, p. 7–59.

Kusakabe, M., Nakagawa, S., Hori, M., Matsihisa, Y., Ojeda, J.M., and Serrano, L., 1984, Oxygen and sulphur isotopic compositions of quartz, anhydrite, and sulfide minerals from the El Teniente and Río Blanco porphyry copper deposits, Chile: Bulletin of the Geological Survey of Japan, v. 35, p. 583–614.

Kusakabe, M., Hori, M., Yukihhiro, M., 1990, Primary mineralization-alteration of the El Teniente and Río Blanco porphyry copper deposits, Chile: Stable isotopes, fluid inclusions and $Mg^{2+}/Fe^{2+}/Fe^{3+}$ ratios in hydrothermal biotite: University of Western Australia Publication 2, p. 244–259.

Ohmoto, H., and Goldhaber, M.B., 1997, Sulfur and carbon isotopes, *in* Barnes, H.L., ed., Geochemistry of hydrothermal ore deposits, 3rd ed.: New York, John Wiley and Sons, p. 517–611.

Potter, R.W.I, Clynne, M.A., and Brown, D.L., 1978, Freezing point depression of aqueous sodium chloride solutions: Economic Geology, v. 73, p. 284–285.

Puig, A., 1988, Geologic and metallogenic significance of the isotopic composition of lead in galenas of the Chilean Andes: Economic Geology, v. 83, p. 843–858.

Quirt, S., Clark, A.H., Farrar, E., and Sillitoe, R.H., 1971, Potassium-argon ages of porphyry copper deposits in northern and central Chile [abs.]: Geological Society of America Abstracts with Programs, no. 3, p. 676–677.

Rae, A.J., Cooke, D.R., Phillips, D., Yeats, C., Ryan, C., and Hermoso, D., 2003. Spatial and temporal relationships between hydrothermal alteration assemblages at the Palinpinon geothermal field, Philippines: Implications for porphyry and epithermal ore deposits: Society of Economic Geologists Special Publication 10, p. 223–246.

Robinson, B.W., and Kusakabe, M., 1975, Quantitative preparation of sulfur dioxide, for $^{34}S/^{32}S$ analyses, from sulfides by combustion with cuprous oxide: Analytical Chemistry, v. 47, p. 1179–1181.

Roedder, E., 1984, Fluid inclusions: Reviews in Mineralogy, v. 12, 644 p.

Rye, R.O., 1993, The evolution of magmatic fluids in the epithermal environment: the stable isotope perspective: Economic Geology, v. 88, p. 733–753

Serrano, L., Vargas, R., Stambuk, V., Aguilar, C., Galeb, M., Holmgren, C., Contreras, A., Godoy, S., Vela, I., Skewes, A.M., and Stern, C.R., 1996, The late Miocene to early Pliocene Río Blanco-Los Bronces copper deposit, central Chilean Andes: Society of Economic Geologists Special Publication 5, p.119–130.

Skewes, M.A., and Holmgren, C., 1993, Solevantamiento andino, erosión y emplazamiento de brechas mineralizadas en el deposito de cobre porfídico Los Bronces, chile central (33ºS): aplicación de geothermometria de inclusiones fluidas: Revista Geológica de Chile, v. 20, p. 71–83.

Skewes, M.A., and Stern, C.R., 1996, Late Miocene mineralized breccias in the Andes of central Chile: Sr and Nd isotopic evidence for multiple magmatic sources: Society of Economic Geologists Special Publication 5, p. 119–130.

Skewes, M.A., Holmgren, C., and Stern, C.R., 2003, The Donoso copper-rich, tourmaline-bearing breccia pipe in central Chile: Petrologic, fluid inclusion and stable isotope evidence for an origin from magmatic fluids: Mineralium Deposita, v. 38, p. 2–21.

Tilton, G.R., 1979, Isotopic studies of Cenozoic Andean calc-alkaline rocks: Year Book - Carnegie Institution of Washington Yearbook 78, p. 298–303.

Tosdal, R.M., and Munizaga, F., 1996, Basement influences on ore deposits in the Chilean Andes (30–34ºS) [abs.]: Geological Society of America Abstracts with Programs, v. 28, no. 7, p. 154.

——2003, Lead sources in Mesozoic and Cenozoic Andean ore deposits: North-central Chile (30–34ºS): Mineralium Deposita, v. 38, p. 234–250.

Vargas, R., Gustafson, L.B., Vukasovic, M, Tidy, E., and Skewes, A., 1999, Ore breccias in the Río Blanco-Los Bronces porphyry copper deposit, Chile: Society of Economic Geologists Special Publication 7, p.281–297.

Vergara, M., Charrier, R., Munizaga, F., Rivano, S, Sepulveda, P., Thiele, R., and Drake, R., 1988, Miocene volcanism in the central Chilean Andes (31º30'S-34º35'S): Journal of South American Earth Sciences, v.1, p.199–209.

Warnaars, F.W., Holmgren, C.D., and Barassi, S., 1985, Porphyry copper and tourmaline breccias at Río Blanco-Los Bronces, Chile: Economic Geology, v. 80, p. 1544–1565.

Zentilli, M., Doe, B., Hedge, C.E., Alvarez, C.E., Tidy, E., and Daroca, J.A., 1988, Isótopos de plomo en yacimientos de tipo porfido cuprífero comparados con otros depósitos metalíferos en los Andes del norte de Chile y Argentian: Congreso Geológico Chileno, 5th, Santiago, Augusto 8–12, Actas, p. B331–369.